



# Key Role of Diabatic Processes in Regulating Warm Water Volume

## Variability

### Over ENSO Events

Maurice F. Huguenin \*

Institute for Atmospheric and Climate Science, ETH Zurich, Zurich, Switzerland, Climate

Change Research Centre and ARC Centre of Excellence for Climate System Science, University  
of New South Wales, Sydney, New South Wales, Australia

Ryan M. Holmes

School of Mathematics and Statistics, Climate Change Research Centre and ARC Centre of  
Excellence for Climate System Science, University of New South Wales, Sydney, New South  
Wales, Australia

Matthew H. England

Climate Change Research Centre and ARC Centre of Excellence for Climate System Science,  
University of New South Wales, Sydney, New South Wales, Australia

\*Corresponding author address: Maurice F. Huguenin

E-mail: m.huguenin-virchaux@unsw.edu.au

## ABSTRACT

17 The equatorial Pacific Warm Water Volume (WWV), defined as the volume  
18 of water warmer than 20°C near the Equator, is a key predictor for the El  
19 Niño-Southern Oscillation (ENSO), and yet much about the individual pro-  
20 cesses that influence it remains unknown. In this study, we conduct idealised  
21 ENSO simulations forced with symmetric El Niño- and La Niña-associated  
22 atmospheric anomalies as well as a historical 1979–2016 hindcast simulation.  
23 We use the water mass transformation framework to examine the individual  
24 contributions of diabatic and adiabatic processes to changes in WWV. We find  
25 that in both sets of simulations, El Niño’s discharge and La Niña’s recharge  
26 periods are initiated by diabatic fluxes of volume across the 20°C isotherm  
27 associated with changes in surface forcing and vertical mixing. Changes in  
28 adiabatic horizontal volume transport above 20°C between the Equator and  
29 subtropical latitudes dominate at a later stage. While surface forcing and ver-  
30 tical mixing deplete WWV during El Niño, surface forcing during La Niña  
31 drives a large increase partially compensated for by a decrease driven by ver-  
32 tical mixing. On average, the ratio of diabatic to adiabatic contributions to  
33 changes in WWV during El Niño is about 40% : 60%, during La Niña this ra-  
34 tio changes to 75% : 25%. The increased importance of the diabatic processes  
35 during La Niña, especially the surface heat fluxes, is linked to the shoaling of  
36 the 20°C isotherm in the eastern equatorial Pacific and is a major source of  
37 asymmetry between the two ENSO phases, even in the idealised simulations  
38 where the wind forcing and adiabatic fluxes are symmetric.

<sup>39</sup> **1. Introduction**

<sup>40</sup> The El Niño-Southern Oscillation (ENSO) is a coupled ocean-atmosphere phenomenon in the  
<sup>41</sup> equatorial Pacific that dominates variability in the Earth's climate system on the interannual time  
<sup>42</sup> scale. Although ENSO's key dynamics are found in the Pacific, its impacts occur on a global  
<sup>43</sup> scale. The instrumental record of global surface air temperature (SAT) shows the dominant role  
<sup>44</sup> of ENSO during recent periods of warming and cooling (Trenberth et al. 2007; Hartmann et al.  
<sup>45</sup> 2013). High sea surface temperature (SST) values in the equatorial Pacific during the 1997–1998  
<sup>46</sup> El Niño increased global SAT by 0.2–0.64°C (depending on the data product, Reynolds et al.  
<sup>47</sup> 2007; Morice et al. 2012), while global SAT decreases during La Niña events (Reynolds et al.  
<sup>48</sup> 2007; Meehl et al. 2011; Roemmich and Gilson 2011).

<sup>49</sup> As a result of its profound socio-economic and environmental impacts (e.g., see Diaz et al. 2001;  
<sup>50</sup> Collins et al. 2010; Timmermann et al. 2018), an increased understanding of ENSO's underlying  
<sup>51</sup> dynamics and key metrics is necessary. Warm water volume (WWV, defined as the volume of  
<sup>52</sup> water above the 20°C isotherm in the equatorial region 120°E–80°W and 5°N–5°S) is one such  
<sup>53</sup> metric, and is commonly used to forecast ENSO events as it leads eastern Pacific SST anomalies  
<sup>54</sup> by 6–8 months (Bosc and Delcroix 2008; McPhaden 2012; Neske and McGregor 2018). Since  
<sup>55</sup> its suggestion as a key ingredient in ENSO dynamics by Wyrtki (1975, 1985), the Warm Water  
<sup>56</sup> Volume has played a key role in many conceptual theories of ENSO, such as the discharge/recharge  
<sup>57</sup> oscillator theory (Suarez and Schopf 1988; Jin 1997a,b; Burgers et al. 2005). In recent decades,  
<sup>58</sup> WWV has been established as an integral component of many analyses, models and statistical  
<sup>59</sup> forecast schemes for ENSO (e.g. Meinen and McPhaden 2000; Izumo et al. 2018; Timmermann  
<sup>60</sup> et al. 2018). However, knowledge of the precise mechanisms influencing WWV remains limited.

61 The goal of this study is to analyse the relative importance of the various processes leading to  
62 changes in WWV.

63 Over a typical ENSO cycle, WWV undergoes discharge and recharge phases resulting from both  
64 adiabatic and diabatic volume fluxes. Adiabatic volume fluxes change WWV through horizontal  
65 transport (above the 20°C isotherm) into or out of the WWV region, or through surface volume  
66 fluxes due to precipitation, evaporation and river runoff (Lengaigne et al. 2012). Diabatic processes  
67 induce WWV changes via water mass transformation (WMT) with heating/cooling of water near  
68 20°C leading to a change in the temperature of that water, and thus a movement of volume across  
69 the 20°C isotherm (Walsh 1982; Large and Nurser 2001; Groeskamp et al. 2019; Holmes et al.  
70 2019a).

71 There are two main diabatic processes that alter WWV; first, the surface heat flux comprising the  
72 radiative, sensible and latent heat fluxes, changes the temperature of water masses in the surface  
73 layers resulting in across-isotherm volume fluxes. The surface heat flux is strongly dependent on  
74 SST, with enhanced heat loss occurring over warm SSTs. During the build-up phase of El Niño  
75 the equatorial Pacific accumulates heat, which following the peak of the event is subsequently  
76 discharged to extratropical latitudes where it is radiated back into the atmosphere or into space  
77 (Trenberth et al. 2002) but also discharged into deeper ocean layers (Roemmich and Gilson 2011;  
78 Johnson and Birnbaum 2017; Wu et al. 2019). The other important diabatic process relates to  
79 small-scale turbulent mixing, which can also drive significant across-isotherm volume fluxes. Tur-  
80 bulent mixing is an important component of the cold tongue SST budget and contributes to changes  
81 in SST over a range of time scales (Moum et al. 2013; Bernie et al. 2005). Strong turbulence in the  
82 equatorial Pacific associated with the large vertical shear above the eastward flowing equatorial un-  
83 dercurrent (EUC) mixes the warmer surface waters with cold upwelled waters (Smyth and Moum  
84 2013) and, depending on depth, leads to diabatic volume exchanges across the 20°C isotherm.

85 This turbulence also plays an important role in the global ocean's heat budget by moving heat  
86 into deeper, colder layers that connect with the deep ocean's overturning circulation (Holmes et al.  
87 2019b). The dynamics of upper equatorial turbulence are complex, being influenced by processes  
88 such as the diurnal cycle, tropical instability waves, the seasonal cycle, equatorial Kelvin waves  
89 and ENSO events themselves (Gregg et al. 1985; Lien et al. 1995; Smyth and Moum 2013; Holmes  
90 and Thomas 2015; Pham et al. 2017; Warner and Moum 2019). Additionally, a third diabatic vol-  
91 ume flux arises in numerical climate models: numerical mixing, emerging from truncation errors  
92 in the model's advection scheme (Holmes et al. 2019a).

93 While the role of adiabatic fluxes during discharge and recharge periods is relatively well un-  
94 derstood based on data from the Tropical Atmosphere and Ocean Array (e.g., see Meinen and  
95 McPhaden 2000, 2001) and modelling studies (e.g., see McGregor et al. 2013, 2014), much about  
96 the diabatic processes remains unknown and will be the focus here. While studies by Meinen  
97 and McPhaden (2000); Clarke et al. (2007) and Lengaigne et al. (2012) agree that diabatic pro-  
98 cesses are important contributors to WWV changes, the observation-based study by Bosc and Del-  
99 croix (2008) and the modelling study by Brown and Fedorov (2010) suggest that diabatic volume  
100 changes on ENSO-related time scales are negligible, thus highlighting the importance for further  
101 analyses with other models and data sets. Lengaigne et al. (2012) suggests that diabatic fluxes  
102 may also explain some of the asymmetries and non-linearities in ENSO's underlying dynamics,  
103 highlighting the need for a more in-depth analysis of the WWV budget in an idealised setting  
104 where asymmetries are controlled. In most studies so far, either vertical (and in modelling studies  
105 additionally numerical) mixing or both surface forcing and vertical mixing fluxes were inferred by  
106 using a residual. Here, we use the WMT framework (Walsh 1982; Large and Nurser 2001; Holmes  
107 et al. 2019a; Groeskamp et al. 2019) in temperature space applied online within a global ocean

<sup>108</sup> model to diagnose the diabatic terms directly during idealised, symmetric ENSO events as well as  
<sup>109</sup> during a hindcast simulation over the 1979–2016 period.

<sup>110</sup> The rest of this paper is organised as follows: in Section 2, the ocean models, atmospheric  
<sup>111</sup> forcing and experimental design are described. To simulate idealised ENSO events and exam-  
<sup>112</sup> ine asymmetries, an approach using Empirical Orthogonal Functions (EOFs) similar to McGregor  
<sup>113</sup> et al. (2014) is used. In Section 3 we discuss ocean-sourced asymmetries in standard ENSO met-  
<sup>114</sup> rics arising in these idealised simulations where the atmospheric forcing is symmetric. Section 4  
<sup>115</sup> introduces the theoretical aspects of the WWV budget and how it is diagnosed within the mod-  
<sup>116</sup> els. After investigating the climatological WWV budget in Section 5, we take a closer look at the  
<sup>117</sup> anomalies during the idealised discharge and recharge phases of ENSO (Section 6). We then com-  
<sup>118</sup> pare the WWV budget terms from the idealised simulations to the event-to-event variability over  
<sup>119</sup> the 1979–2016 period (Section 8) before summarising our results and their implications (Section  
<sup>120</sup> 9).

## <sup>121</sup> 2. Model, Data and Methods

### <sup>122</sup> a. The Ocean-Sea Ice Model

<sup>123</sup> In this study, we use a  $1/4^\circ$  global ocean model with 50  $z^*$  vertical levels based on the ocean  
<sup>124</sup> component of the Geophysical Fluid Dynamics Laboratory (GFDL) CM2.5 coupled climate model  
<sup>125</sup> (Delworth et al. 2012; Griffies 2012). Atmospheric forcing for the model is derived from a pre-  
<sup>126</sup> scribed atmospheric state (Sections 2b and 2c) using eight fields to calculate zonal and meridional  
<sup>127</sup> wind stress, and surface heat and freshwater fluxes using bulk formulae (Fairall et al. 1996). The  
<sup>128</sup> eight atmospheric fields are zonal and meridional wind speed, air temperature and specific humid-  
<sup>129</sup> ity at 10 m, and downward long- and short-wave radiation, precipitation and sea level pressure

130 at the ocean's surface. Vertical diffusion is parameterised using the K-profile parameterisation  
131 scheme (KPP, Large et al. 1994). The model can be considered eddy-resolving in the tropics  
132 (Hallberg 2013; Jochum et al. 2008). In the baseline model, there is no explicit horizontal dif-  
133 fusion of tracer gradients and thus sharp lateral tracer gradients are smoothed by the numerical  
134 advection scheme. The associated diffusion is termed ‘numerical mixing’ as discussed further in  
135 Section 4 and in Holmes et al. (2019a). More information and discussion on the model details, dif-  
136 fusive mixing parameterisations and the model performance can be found in Spence et al. (2017),  
137 Stewart et al. (2017) and Holmes et al. (2019a).

138 *b. Forcing for the Idealised, Symmetric Simulations*

139 For the idealised simulations, the model was spun-up over a 500–year period using the climato-  
140 logical Coordinated Ocean-ice Reference Experiment Normal Year Forcing (CORE-NYF, Large  
141 and Yeager 2004). For our idealised simulations, we add ENSO-related perturbations derived from  
142 the European Centre for Medium-Range Weather Forecasts’ (ECMWF’s) ERA-Interim product for  
143 1979–2016 (Dee et al. 2011) to the base CORE-NYF fields.

144 Our perturbation experiments are constructed to isolate the most important aspects of ENSO  
145 variability in the atmospheric forcing (as quantified by the leading two EOFs of monthly tropical  
146 Pacific wind stress variability) to isolate oceanic-sourced asymmetries. Following the approach  
147 by McGregor et al. (2013, 2014), we first regress NOAA’s ERSST v4 Niño3.4 (N34) index (Smith  
148 and Reynolds (2003), calculated as the SST deviation in the equatorial region 170°W–120°W and  
149 5°N–5°S) onto the ERA-Interim wind stress anomalies from 1979–2016. This regression yields  
150 the spatial pattern of wind stress anomalies that are linearly associated with El Niño ( $X_{1,\tau}$ , Fig.  
151 1a). This pattern captures the weakening of the Walker circulation during an El Niño event and is  
152 characterised by westerly wind stress anomalies in the western tropical Pacific, with slightly larger

values in the Southern Hemisphere. Calculating the first EOF of equatorial wind stress anomalies instead of regressing N34 gives a time series which is highly correlated with N34 (correlation coefficient  $r = 0.76$ ). As in McGregor et al. (2014) we use the smoother N34 time series here. This first mode captures 58.6% of the wind stress variability in the equatorial region.

To calculate the second pattern, the anomalies associated with  $X_{1,\tau}$  and N34 are removed from the wind stress anomaly time series at each spatial location and the first EOF of the residual wind stress over the tropical Pacific region  $100^{\circ}\text{E}–60^{\circ}\text{W}$  and  $10^{\circ}\text{N}–10^{\circ}\text{S}$  is calculated (as in McGregor et al. 2014). The resulting wind stress pattern ( $X_{2,\tau}$ , Fig. 1b) and its associated principle component time series, (PC2, Fig. 1c) capture a strong meridional gradient of zonal wind anomalies across the Equator and play a crucial role in the winds' non-linearity related to ENSO (Zeller et al. 2019). This mode gains importance when it changes sign during the peak of El Niño and initiates a southward shift of the westerly wind anomalies (Fig. 1c, McGregor et al. 2013; Stuecker et al. 2013). The resulting Ekman-induced transport is much higher in the Northern than in the Southern Hemisphere, leading to an equatorial divergence of water masses (McGregor et al. 2014; Stuecker et al. 2015; Timmermann et al. 2018). This second mode drives 17.1% of the variability within the residual wind stress anomalies and combined, the first two EOF patterns explain 75.7% of the total wind stress variability within the ERA-Interim data set.

McGregor et al. (2014) used the two time series N34 and PC2 (Fig. 1c) from observations to simulate the variability of the tropical Pacific over the time period 1979–2011. Instead of using the full time series, we construct idealised synthetic time series for N34 and PC2 from the three strongest El Niño events as a basis to simulate isolated symmetric El Niño and La Niña events (i.e. we only use the time series during the red shaded periods in Fig. 1c). For our first experiments, the evolution of N34 and PC2 during the three strongest El Niño events for 1979–2016 are composited and centered at their peak in December (i.e. month 12, Fig. 2). Fourth-order polynomials are fitted

177 to the mean of these three events so that anomalies increase from zero amplitude and slowly evolve  
178 in a way that approximates the mean of the three strong ENSO events (bold lines in Fig. 2). The  
179 polynomials are constrained to start close to zero, thereby requiring minimal adjustment at the  
180 beginning in order to achieve a smooth event onset. In addition, the N34 time series is adjusted to  
181 slowly return to zero during a spin-down period of two years following the event (Months 24–48),  
182 while the PC2 time series is zero during the full spin-down period (Fig. 2). We also simulate  
183 a symmetric ‘La Niña’ event, where the time series are simply set to negative amplitude with  
184 respect to the El Niño case. This allows us to investigate any asymmetric responses resulting from  
185 ocean-sourced non-linearities in the presence of symmetric atmospheric forcing.

186 The atmospheric fields that force the model are then derived using regressions of the N34 index  
187 and PC2 time series as described in the Appendix. To increase the signal-to-noise ratio, ensemble  
188 simulations were also performed. However we found that differences between the ensemble mem-  
189 bers are more than two orders of magnitude smaller than the variability in the ensemble mean,  
190 and so we only present results from one ensemble member. We calculate the anomalies relative to  
191 the time-mean fields of eight years in the control simulation, except for ocean heat content where  
192 we subtract the time-varying control simulation to better account for the drift in the 200–2000 m  
193 layers.

#### 194 c. Interannual Model Simulation

195 We follow-up our idealised, symmetric ENSO simulations with an interannual hindcast simu-  
196 lation for the period 1979–2016 with an updated configuration of the model (Kiss et al. 2020).  
197 The forcing for this configuration is from the JRA55-do v1.3 reanalysis for 1958–2018 (Tsujino  
198 et al. 2018) and the spin-up was performed by using five repeat cycles of JRA55-do (Kiss et al.  
199 2020). The resolution and model physics in this configuration are identical to the base model, ex-

cept that it uses an updated 50-level vertical grid and it includes the Gent and McWilliams (1990) parameterisation for mesoscale eddies as well as explicit Redi (1982) along-isopycnal diffusion. However, these parameterisations are scaled with latitude and neither plays an important role in the tropics. For our analysis, we analyse the 1979–2016 period of the last cycle where the online WMT diagnostics are output.

### 3. ENSO's Ocean-Sourced Anomalies During Idealised Events

In this section, we first discuss the ocean-sourced anomalies and asymmetries in our idealised symmetrically-forced El Niño and La Niña simulation before presenting an in-depth analysis of the WWV budget in the following sections.

Although ENSO's anomalies are strongest in the Pacific, they have impacts on a global scale (e.g. Roemmich and Gilson 2011; Wu et al. 2019; Cheng et al. 2019). Global mean sea surface temperature (GMSST) anomalies during the strong El Niño 1997–1998 exceeded 0.2°C in NOAA's OI SST V2 data set (Reynolds et al. 2007; Roemmich and Gilson 2011). This is mostly caused by the warm eastern equatorial Pacific during El Niño. In our idealised El Niño simulation, maximum GMSST anomalies are reached in December, with a value of 0.092°C (blue line, Fig. 3a). These anomalies are lower than the 0.2°C in NOAA's OI SST v2 product, but expected as our idealised simulation is based on a composite events.

The N34 index explains a large part of the increase in GMSST (light blue line in Fig. 3c). The maximum value of the N34 index (1.57°C), is slightly lower than given by the idealised time series (dashed line Fig. 3c), which is not unexpected since SST is determined dynamically within the model. In the last four months of the El Niño event (months 20–24), both the idealised and modelled N34 anomalies are negative, indicating a change to developing La Niña-like conditions. This represents the discharged state of the tropical Pacific at the end of the El Niño event. To first

order, the anomalies in the La Niña simulation (Fig. 3b, d) are opposite to the El Niño event. In particular, the N34 index and GMSST anomalies are close to the exact opposite during La Niña, with only a slightly increased amplitude (Fig. 3).

The rate of change of the ocean's heat content (OHC) is highest when both GMSST and the N34 index peak at month 12 (orange line, Fig. 3a). As expected, this suggests that the warmest equatorial Pacific SST values coincide with the highest anomalous surface heat fluxes into the atmosphere or into space during El Niño (and opposite for month 12 during La Niña in Fig. 4, as in Meinen and McPhaden 2001; Johnson and Birnbaum 2017; Cheng et al. 2019). The global ocean's heat release continues until month 20 of the simulation when equatorial SSTs and surface heat fluxes return to neutral conditions. The WWV anomalies as a proxy for the upper equatorial OHC show a similar behaviour as the global OHC anomalies, with discharge during El Niño lasting 15 months and recharge occurring over a period of 14 months during La Niña (red line, Fig. 3c, d). Unlike OHC, the anomalous WWV time series shows a considerable positive and negative peak prior to the peak of El Niño and La Niña. This behaviour is caused by the first EOF mode of wind stress anomalies initiating an equatorward surface Ekman transport during El Niño, while causing a poleward transport during La Niña (McGregor et al. 2014). The surface Ekman transport during this stage is more dominant than the subsurface geostrophic transport of the opposing sign, effectively causing a recharge and discharge of WWV (McGregor et al. 2014). The global OHC anomalies do not show this distinct increase or decrease prior to the peak of the events. The WWV anomalies before the discharge phase (Fig. 3c) are lower compared to those in Meinen and McPhaden (2000) and likely caused by the weaker build-up prior to the event due to the transition from climatological forcing.

Additionally, our idealised experimental design also contains the following simplifications that could each contribute to deviations from observed events: (1) we use NOAA's ERSST v4 N34

247 index as in McGregor et al. (2014) to derive the atmospheric forcing. This index, in particular  
 248 during strong El Niño events, is weaker than the same index in the ERA-Interim reanalysis (Dee  
 249 et al. 2011) and HadISST (Rayner et al. 2003) products as it has larger parametric uncertainties  
 250 at smaller spatial and shorter time scales (including for ENSO events, Liu et al. 2015; McGregor  
 251 et al. 2017). (2) We force the model in these simulation with an interpolated atmospheric field  
 252 from monthly-averaged anomalies and a grid resolution of 220 km, and thus do not fully cap-  
 253 ture high-frequency variability such as westerly wind events, which are known to impact WWV  
 254 anomalies (Menkes et al. 2014). (3) In our simulations, we use only the first two EOF modes  
 255 of equatorial wind stress anomalies associated with El Niño which account for 75% of the total  
 256 variance. Despite these approximations, the idealised simulations are able to reproduce the key  
 257 physical processes throughout ENSO.

#### 258 4. The Warm Water Volume Budget

259 In this section we give a brief theoretical introduction into the WWV budget and how it is  
 260 constructed within the model experiments. We define WWV as the volume of water above the  
 261 20°C isotherm in the area between Borneo ( $116^{\circ}30'E$ ), the South American coastline ( $78^{\circ}W$ ) and  
 262  $5^{\circ}N$ – $5^{\circ}S$ . This WWV definition has been previously used in studies by Meinen and McPhaden  
 263 (2000), Lengaigne et al. (2012), McGregor et al. (2014) and others. We define the Indonesian  
 264 Throughflow (ITF) as the transport between Borneo ( $116^{\circ}30'E$ ) and New Guinea ( $133^{\circ}45'E$ ) at  
 265  $2^{\circ}S$ .

266 In order to understand and diagnose the WWV budget, we not only evaluate horizontal adiabatic  
 267 volume fluxes, but also evaluate how volume is exchanged vertically across the 20°C isotherm.  
 268 Across-isotherm volume fluxes can be studied by using the WMT framework, first introduced by

269 Walin (1982). It describes the processes that lead to a given water parcel's change in temperature  
270 and subsequent movement across isotherms.

271 Changes in WWV over time are dependent on both adiabatic and diabatic processes:

$$\frac{dWWV}{dt} = \underbrace{\mathcal{T}_{5^{\circ}N+5^{\circ}S} + \mathcal{T}_{ITF}}_{\text{Adiabatic processes}} + \underbrace{\mathcal{J} + \mathcal{G}_F + \mathcal{G}_M + \mathcal{G}_I}_{\text{Diabatic processes}}, \quad (1)$$

272 where  $dWWV/dt$  is the WWV tendency [ $\text{m}^3 \text{ s}^{-1}$ ], calculated by using snapshots of the temper-  
273 ature field at the beginning and end of each month (the period over which the right-hand side  
274 diagnostics in Equation 1 are accumulated online). The adiabatic processes include the lateral  
275 transport of water masses above  $20^{\circ}\text{C}$  into and out of the WWV region across the three transects  
276  $5^{\circ}\text{N}, 5^{\circ}\text{S}$  ( $\mathcal{T}_{5^{\circ}N+5^{\circ}S}$ ), and the ITF ( $\mathcal{T}_{ITF}$ ) [ $\text{m}^3 \text{ s}^{-1}$ ]. In addition, the surface volume flux  $\mathcal{J}$  [ $\text{m}^3 \text{ s}^{-1}$ ]  
277 accounts for small adiabatic volume changes due to river runoff, precipitation, and evaporation of  
278 water above  $20^{\circ}\text{C}$  when freshwater enters or leaves the ocean at the sea surface. The surface vol-  
279 ume fluxes in the model enter and exit the ocean at the sea surface temperature (Holmes et al.  
280 2019a). Thus, there is no additional sensible heat flux into the ocean associated with differences  
281 in temperature between the freshwater and the surface sea water. Therefore, in the model, these  
282 fluxes are considered adiabatic. These adiabatic variables are diagnosed by summing the associ-  
283 ated transports over all temperature classes warmer than  $20^{\circ}\text{C}$ . The calculations (i.e. the binning  
284 into temperature classes) take place online at every time step of the model simulation. Here we  
285 show the monthly accumulated averages of these online diagnostics.

286 The three diabatic WMT volume fluxes include surface forcing  $\mathcal{G}_F$ , vertical mixing  $\mathcal{G}_M$  and  
287 numerical mixing  $\mathcal{G}_I$ , each expressed in units of [ $\text{m}^3 \text{ s}^{-1}$ ]. The surface forcing volume flux  $\mathcal{G}_F$   
288 across the  $20^{\circ}\text{C}$  isotherm is driven by the surface heat flux and its different components (short-  
289 wave, long-wave, sensible and latent heat fluxes).  $\mathcal{G}_F$  is the convergence of these heat fluxes  
290 within a given temperature class, which indicates fluid warming and therefore crossing isotherms

toward warmer or colder fluid. Likewise,  $\mathcal{G}_{\mathcal{M}}$  is the WMT volume flux arising from parameterised diffusive vertical mixing processes. Through heating and cooling fluid, diffusive mixing likewise moves water across temperatures classes. These two WMT fluxes are calculated as diagnostics from the heat budget binned into temperature space (Holmes et al. 2019a), and depend on the across-isotherm heat fluxes through,

$$\mathcal{G}_{\mathcal{F}} = \frac{1}{\rho_0 \cdot C_p} \cdot \int \int \left. \frac{\partial \mathcal{F}}{\partial \Theta} \right|_{20^\circ C} dA, \quad (2)$$

$$\mathcal{G}_{\mathcal{M}} = \frac{1}{\rho_0 \cdot C_p} \cdot \int \int \left. \frac{\partial \mathcal{M}}{\partial \Theta} \right|_{20^\circ C} dA. \quad (3)$$

Here,  $\rho_0$  is the reference density of sea water ( $1035 \text{ kg m}^{-3}$ ),  $C_p$  is the specific heat capacity of sea water at constant pressure ( $3992.1 \text{ J kg}^{-1} \text{ K}^{-1}$ ) and  $\mathcal{F}$  is the total surface heat flux [ $\text{W m}^{-2}$ ] into all fluid warmer than a given potential temperature  $\Theta$  at each horizontal location (taking into account the penetration of short-wave radiation into the interior). Similarly,  $\mathcal{M}$  is the total heat flux into all fluid warmer than  $\Theta$  at each horizontal location due to vertical diffusion and the non-local heat flux component of the KPP boundary layer mixing scheme [ $\text{W m}^{-2}$ ] of Large and Yeager (2004), although this non-local term plays a minor role. Both  $\mathcal{F}$  and  $\mathcal{M}$  are diagnosed online by binning the corresponding Eulerian heat budget diagnostics into temperature classes at every time step. The temperature bin size is  $0.5^\circ \text{C}$ . We evaluate the WWV budget at  $20^\circ \text{C}$  and the area integral is performed over the WWV region ( $116^\circ 30' \text{E} - 78^\circ \text{W}$  and  $5^\circ \text{N} - 5^\circ \text{S}$ ). More details on the numerical implementation of these WMT diagnostics are presented in Holmes et al. (2019a).

Lastly, the WMT flux  $\mathcal{G}_{\mathcal{I}}$  arises from numerical diffusion associated with truncation errors in the model's tracer advection scheme (i.e. numerical mixing). The advection scheme is three-dimensional and acts to smooth both vertical and horizontal tracer gradients at the grid scale (Colella and Woodward 1984). Due to choices made to minimise sources of explicit diffusion (namely, zero explicit lateral diffusion or background vertical diffusivity), numerical dif-

313 fusion makes a non-negligible contribution to the global climatological heat budget (Holmes et al.  
314 (2019a); their Fig. 3) and the WWV budget. We calculate  $\mathcal{G}_{\mathcal{T}}$  as the residual of Equation 1.

315 The WWV budget additionally includes terms associated with the parameterisation of subme-  
316 soscalscale eddies (Fox-Kemper et al. 2008) and, in the 1979–2016 hindcast simulation, mesoscale  
317 eddies (Redi 1982; Gent and McWilliams 1990). These fluxes make negligible contributions to  
318 the WWV budget but are included in our calculation as  $\mathcal{G}_{\mathcal{E}}$  (eddy mixing) in order to accurately  
319 calculate numerical mixing as the residual.

## 320 5. The Climatological Warm Water Volume Budget

321 Before our analysis of the anomalous WWV budget terms during ENSO, we first investigate its  
322 climatology as the anomalous fluxes are tightly linked to the seasonal cycle.

323 The climatological WWV in the control simulation exhibits a small long-term spin-up trend of  
324  $9.1 \times 10^{12} \text{ m}^3 \text{ yr}^{-1}$  (equivalent to 0.28 Sv). It is closely linked to the equatorial overturning cir-  
325 culation and comprises a balance between the adiabatic and diabatic fluxes. Vertical mixing in  
326 the annual mean cools surface water masses and simultaneously warms deeper layers, represented  
327 by the negative (blue) and positive (red) across-isotherm (or diathermal) velocity regions in Fig.  
328 4a. Surface forcing is consistently warming the surface region (Fig. 4b). The annual mean 20°C  
329 isotherm is positioned on average in the warming region of both diabatic fluxes, indicating a net  
330 upward volume flux across the isotherm into the WWV above. Thus, vertical mixing (+6.7 Sv,  $\text{Sv}$   
331  $= 10^6 \text{ m}^3 \text{ s}^{-1}$ ) and surface forcing (+2.7 Sv) both show positive contributions to the annual mean  
332 budget. Numerical mixing plays only a minor role. The convergent diathermal transport is bal-  
333 anced by negative contributions from the predominantly eastward trade winds driving a divergent  
334 Ekman transport across 5°N and 5°S ( $-6.1 \text{ Sv}$ ) and transport through the ITF ( $-6.2 \text{ Sv}$ , Schott  
335 et al. 2004). The impact of the surface volume flux is negligible compared to the other terms (as

336 in Meinen and McPhaden 2001; Lengaigne et al. 2012; Brown and Fedorov 2010) and will not be  
337 discussed further.

338 These processes (both adiabatic and diabatic) have a seasonal cycle linked to the strength of the  
339 equatorial trade winds (Horel 1982). The WWV peaks near the end of the year, increasing in the  
340 second half of the year, and decreasing in the first half (black line Fig. 5a). While meridional  
341 transport explains part of the WWV recharge in the second half of the year, most of this increase  
342 stems from the enhanced diabatic fluxes (Fig. 5b). The stronger trade winds in the second half  
343 of the year increase upwelling of cold water masses, shoaling of the 20°C isotherm and heat  
344 absorption from the atmosphere (Fig. 4d). At the same time, shear- and wind-driven turbulence  
345 in the upper EUC intensifies, driving stronger diabatic upwelling via vertical mixing across the  
346 shallower 20°C isotherm (Fig. 4c, Moum et al. 2013; Liu et al. 2016). Combined, the two diabatic  
347 fluxes result in positive diathermal velocities across the 20°C isotherm in the eastern equatorial  
348 Pacific and an increase in WWV (i.e. the sum of Fig. 4c and d results in an overall positive, red  
349 spatial pattern). Further, the stronger trade winds also cause an increased sea surface height (SSH)  
350 difference between the Indian and Pacific Ocean leading to an increased strength of the ITF, which  
351 partially offsets the two diabatic fluxes in the second half of the year (green line, Fig. 5a, Shinoda  
352 et al. 2012).

## 353 6. The Warm Water Volume Budget During Idealised ENSO Events

354 We now examine the anomalous WWV budget terms and asymmetries during the idealised,  
355 symmetric events before comparing them to events in the hindcast simulation. Over the ENSO  
356 cycle, WWV undergoes changes associated with the recharge and discharge of heat. We define the  
357 discharge phase during the idealised El Niño as the period when the WWV anomaly is decreasing,  
358 i.e. the rate of change in WWV is negative (red shaded period from month 7–21, Fig. 6a, c). To

359 ensure a symmetric analysis, we define the recharge phase during La Niña as the same time period  
360 (blue shading, Fig. 6b, d). The anomalies are calculated by subtracting off the climatological  
361 budget discussed in the previous section.

362 *a. The Idealised Symmetric El Niño Discharge*

363 The discharge phase during El Niño is initiated in July when the rate of change in the WWV  
364 anomaly becomes negative (Fig. 6a). WWV depletion in this simulation thus starts five months  
365 ahead of the peak of El Niño and leads over the 15-month period to a total volume decrease of  $2.5 \times$   
366  $10^{14} \text{ m}^3$  (corresponding to 6.3 Sv or a shoaling of the 20°C isotherm by 12.8 m when averaged  
367 over the WWV region). Depletion of WWV occurs in two phases, with an initial decrease driven  
368 mainly by diabatic fluxes across the 20°C isotherm (approximately months 7–14) followed by a  
369 period with dominant horizontal adiabatic transport out of the equatorial region (approximately  
370 months 12–21, red area, Fig. 6a, c).

371 Changes in surface forcing and vertical mixing drive the initial phase of WWV decrease (blue  
372 lines, Fig. 6c). This is consistent with the observation-based study by Meinen and McPhaden  
373 (2001) where there are suggestions that the WWV discharge due to diabatic processes (inferred  
374 as the residual of the WWV change minus the lateral transport) is dominant in the early part of  
375 the 1997 El Niño (e.g. Fig. 13 of Meinen and McPhaden 2001). However, uncertainties in their  
376 calculations are large (estimated as  $\pm 6$  Sv). This highlights the need for future observation-based  
377 studies to better reconcile the role of the observed diabatic, vertical fluxes. The weaker trade  
378 winds during El Niño reduce upwelling of cold water masses to the surface, decrease shear- and  
379 wind driven mixing and deepen the 20°C isotherm. These effects combined result in an overall  
380 reduced/anomalous surface forcing and vertical mixing flux across the 20°C isotherm compared  
381 to climatological conditions (compare Figs. 7a and 4c).

382 The reduced surface forcing and vertical mixing fluxes until the peak of El Niño agree well with  
 383 the observational study by Warner and Moum (2019). Numerical mixing anomalies play a minor  
 384 role throughout the discharge phase contributing only 4% to the overall changes in WWV (Fig.  
 385 8a). Together, the total diabatic volume flux throughout the discharge phase amounts to a volume  
 386 change of  $-1.1 \times 10^{14} \text{ m}^3$ , contributing  $\sim 45\%$  to the total change (Fig. 8a), and is comparable to  
 387 the average estimate over the 1976–2004 time period in Lengaigne et al. (2012).

388 The second phase of WWV discharge occurs about six months later, with meridional transport  
 389 as the dominant driver (red line in Fig. 6a). During the initial discharge phase (months 7–11),  
 390 anomalous adiabatic transport through  $5^\circ\text{N}$  and  $5^\circ\text{S}$  opposes WWV depletion by off-equatorial  
 391 westerly wind bursts, moving more warm water into the equatorial band (McGregor et al. 2016).  
 392 The high amplitude of the first EOF mode (Fig. 1a) combined with the positive amplitude of the  
 393 second EOF mode (Fig. 1b) of wind stress anomalies during the second year of the simulation  
 394 drive a strong Ekman divergence and geostrophic transport of warm water masses across  $20^\circ\text{C}$  to  
 395 higher latitudes (McGregor et al. 2012, 2014; Zeller et al. 2019).

396 While the large-scale horizontal transport through  $5^\circ\text{N}$  and  $5^\circ\text{S}$  during the second phase of dis-  
 397 charge is high, the strength of the ITF is decreased throughout the full discharge phase (green line  
 398 in Fig. 6a, which is slightly positive throughout the time period). This is the result of the reduced  
 399 SSH gradient between the Indian and the Pacific Ocean during El Niño (Sprintall and Révelard  
 400 2014; Feng et al. 2018). Including the ITF, the total adiabatic transport during the discharge period  
 401 contributes  $1.4 \times 10^{14} \text{ m}^3$ , or about 55%, to the total WWV changes (Fig. 8a). During this second  
 402 phase (months 11–21), the diabatic volume fluxes play only a minor role.

403 The change to La Niña-like conditions at the end of the discharge phase concurrent with the  
 404 negative amplitude of the idealised N34 index (black line, Fig. 2) is also evident here in the  
 405 increase in WWV (months 20–24, Fig. 3a). This is caused by the shallower  $20^\circ\text{C}$  isotherm and

<sup>406</sup> colder SST values in the eastern Pacific, leading to increased ocean heat absorption around the  
<sup>407</sup> 20°C isotherm as indicated by an increase in the surface forcing term (dark blue line, Fig. 3a).

<sup>408</sup> *b. The Idealised Symmetric La Niña Recharge*

<sup>409</sup> As during El Niño, the change in WWV during La Niña occurs over two stages. The initial  
<sup>410</sup> phase is dominated by diabatic volume fluxes and the latter half of the recharge phase is mainly  
<sup>411</sup> controlled by meridional transport (Fig. 6b, d). During La Niña's recharge, the total change in  
<sup>412</sup> WWV (i.e. blue region in Fig. 6b, d) is  $2.9 \times 10^{14} \text{ m}^3$ , slightly higher than the change in volume  
<sup>413</sup> during El Niño's discharge phase (Fig. 8b) despite the symmetric atmospheric forcing (this is  
<sup>414</sup> equivalent to a discharge of 7.4 Sv or a deepening of the 20°C isotherm by about 15 m when  
<sup>415</sup> averaged over the WWV region). It is likely caused by the ocean being able to absorb more heat  
<sup>416</sup> when conditions are cool in contrast to El Niño's heat loss.

<sup>417</sup> Compared to El Niño's discharge phase, not all volume fluxes are opposite and of the same  
<sup>418</sup> magnitude. The most striking differences lie in the vertical mixing and surface forcing fluxes  
<sup>419</sup> (compare blue curves in Figs. 6c and 6d). The strengthened trade winds during La Niña drive  
<sup>420</sup> increased vertical mixing in the upper ocean (Fig. 7c, Warner and Moum 2019), yet counter-  
<sup>421</sup> intuitively, the vertical mixing volume flux does not increase but decreases WWV (i.e. in the  
<sup>422</sup> same sense as during El Niño events). This remarkable asymmetry is a result of the strong non-  
<sup>423</sup> linearity associated with shifts in the 20°C isotherm position. Specifically, the shoaling of the  
<sup>424</sup> 20°C isotherm in the eastern equatorial Pacific moves the isotherm from the subsurface, where  
<sup>425</sup> mixing warms water, toward the surface where mixing cools water masses (Fig. 7c, 8b). This  
<sup>426</sup> leads to a downward volume flux across the 20°C isotherm due to mixing throughout much of the  
<sup>427</sup> eastern Pacific toward cooler and deeper layers, and thus a decrease of WWV.

428 In contrast, the surface forcing volume flux clearly dominates WWV build-up, with a much  
429 stronger response compared to El Niño's discharge period. The increased trade wind strength,  
430 the shallower 20°C isotherm (where it is more strongly influenced by surface forcing) and the  
431 cold SST values lead to a high anomalous heat absorption in the eastern equatorial Pacific. This  
432 warm water is then subsequently advected westward and accumulates in the western Pacific warm  
433 pool, deepening the 20°C isotherm there (Fig. 7d). The total contribution of the surface forcing  
434 volume flux to the WWV increase is  $3.7 \times 10^{14} \text{ m}^3$  (128% of the total change in WWV). However,  
435 as the vertical mixing contribution opposes this surface forcing volume flux, the overall diabatic  
436 volume transport accounts for  $\sim 62\%$  (Fig. 8b). This interplay between strong vertical mixing and  
437 strong surface forcing fluxes during the transition to the peak of La Niña is also supported in the  
438 observational study by Warner and Moum (2019). Numerical mixing during La Niña's recharge  
439 phase, as during El Niño's discharge of heat, again plays only a minor role (purple line in Fig. 6c,  
440 d). It contributes only  $\sim 1\%$  to the changes in WWV (Fig. 8b).

441 Contrary to the vertical fluxes, meridional transport into the WWV region during the recharge  
442 phase is largely symmetric with respect to El Niño's discharge. This is caused by the prescribed  
443 symmetric wind stress perturbations, which drive most of the adiabatic transport (see e.g. McGregor  
444 et al. 2012, 2014; Zeller et al. 2019). The small asymmetry in the adiabatic transport relative  
445 to the idealised El Niño may be related to differences in the 20°C isotherm depth capturing a dif-  
446 ferent fraction of the geostrophic return flow despite symmetric wind stress forcing. Consistent  
447 with the recharge oscillator theory, Meinen et al. (2001) and McGregor et al. (2014), horizontal  
448 transport lags the peak SST/wind stress anomalies (roughly when the WWV changes are largest)  
449 by about four months. The ITF is consistently stronger than normal throughout the full recharge  
450 period (green line in Fig. 6b), as strong trade winds increase the SSH in the western equatorial  
451 Pacific, driving higher transport into the Indian Ocean. In total, the adiabatic horizontal transport

452 (and surface volume flux) is responsible for  $\sim$ 38% of the total recharge as compared to the  $\sim$ 55%  
453 contribution during El Niño's discharge (Fig. 8b).

454 In summary, we see that the meridional, adiabatic transport of WWV between the two  
455 symmetrically-forced ENSO phases is largely symmetric. The diabatic processes however are  
456 a considerable source of asymmetry arising from the dependence of the heat fluxes on SST and  
457 the vertical movement of the 20°C isotherm coupled with mixing changes.

458 La Niña events typically last longer and have a reduced amplitude relative to their corresponding  
459 El Niño events as they often re-intensify during the following winter (Okumura and Deser 2010).  
460 Our idealised forcing based on the exact opposite of a composite of El Niño events therefore over-  
461 estimates the magnitude of La Niña. Additionally, La Niña events do not include a clear shift  
462 from negative to positive values in the PC2 time series (red line during red periods, Fig. 1c). It  
463 is therefore important to compare our idealised symmetric simulations to ENSO events and their  
464 event-to-event variability in a simulation with atmospheric forcing more closely following obser-  
465 vations. The next section first validates the 1979–2016 hindcast simulation against observations  
466 before an in-depth analysis of the variability in the WWV budget between events.

## 467 7. ENSO's Ocean-Sourced Anomalies During 1979–2016

468 The simulated N34 index over the 1979–2016 period captures the observed variations in NOAA's  
469 ERSST v4 N34 index (Smith and Reynolds 2003) reasonably well (blue lines, Fig. 9). The three  
470 strong El Niño events in 1982/83, 1997/98 and 2015-16, on which our analysis focuses on, are  
471 slightly overestimated in the simulation compared to the observational time series. As expected,  
472 the anomalous WWV time series leads the N34 index by three to six months (red lines, Fig. 9).  
473 While the correlation between the simulated and observed WWV time series is high ( $r = 0.92$ ),

474 the magnitude is somewhat underestimated during the El Niño in 1997/98 and the La Niña event  
475 2010/11.

476 As the position of the 20°C isotherm is a key factor influencing WWV, it is important to validate  
477 it against observations during El Niño and La Niña events. As mentioned above, a shallow position  
478 increases diabatic WWV transport through enhanced vertical mixing and the penetrating solar heat  
479 fluxes while a deep 20°C isotherm leads to a reduced effect. The climatological position of the  
480 20°C isotherm compares reasonably well to observations (black lines, Fig. 10, Kiss et al. 2020),  
481 although it is slightly shallower west of 140°W (by ~20 m) and deeper (by ~15 m) east of 140°W.  
482 During the 1997–1998 El Niño, as warm water reaches the eastern equatorial Pacific, the 20°C  
483 isotherm in the east deepens by about 120 m in ECMWF's Ocean Reanalysis 5 product (ORA-S5,  
484 Zuo et al. (2018), Fig. 10). The hindcast simulation captures this downward shift of the isotherm,  
485 although with a negative bias of ~30 m around 140°W and a positive bias of ~30 m at 80°W  
486 near the South American coastline. The isotherm position shown in Fig. 10 is the mean over the  
487 September–November period. During the following La Niña in 1998/99, the simulation exhibits a  
488 somewhat too shallow 20°C isotherm in the central Pacific and a negative bias of about 20 to 25 m  
489 in the surface region at 110°W compared to ORA-S5 (blue lines, Fig. 10). These tilt differences in  
490 the isotherm position also occur during other events and likely explain most of the offset between  
491 the simulated and observed anomalous WWV time series in Fig. 9.

## 492 8. The Warm Water Volume Budget During 1979–2016

493 Over the 38-year period between 1979–2016, the equatorial Pacific undergoes multiple dis-  
494 charge and recharge phases of WWV (red shaded and blue shaded periods, Fig. 11). While there  
495 are more than three El Niño and La Niña events during this period, our analysis here will focus

496 on three strong events each. We define these discharge and recharge events as when the rate of  
497 change in WWV anomalies (black line in Fig. 11a) is negative and positive respectively.

498 During El Niño, discharge peaks between 22 and 27 Sv and is much stronger than the 11 Sv in  
499 the idealised simulation (Fig. 9a). As a consequence, the overall total change in WWV associated  
500 with these events is much larger ( $3.5$  to  $5.5 \times 10^{14}$  m $^3$  compared to the  $2.5 \times 10^{14}$  m $^3$  in Fig.  
501 8a). The length of the discharge phases (red shaded period in Fig. 11) is largely constant between  
502 events and consistent with the length in the idealised El Niño simulation. La Niña events on the  
503 other hand show a larger event-to-event variability in the total change in WWV ( $2.5$  to  $4.2 \times 10^{14}$   
504 m $^3$ ) as well as the length of the recharge period (8 to 15 months, blue shaded period in Fig. 11).

505 *a. First Phase: Diabatic Fluxes*

506 As in the idealised simulation, the initial discharge phase during El Niño is dominated by the  
507 diabatic volume fluxes. Over all three strong El Niño events, both surface forcing and vertical  
508 mixing deplete WWV (light and dark blue lines during the red periods, Fig. 11b). The contribu-  
509 tion of the diabatic fluxes to the total change in WWV over the discharge periods in 1982/83  
510 and 1997/98 is 23% and 38%. For the 1997/98 El Niño event, this value is lower compared to  
511 the 50% in both Lengaigne et al. (2012) and Meinen and McPhaden (2001). However, we expect  
512 differences compared to Lengaigne et al. (2012) arising from the temporal filtering (Lengaigne et  
513 al. 2012 use a 16 month–8 year band pass filter while we employ a five-month running mean) as  
514 well as model and forcing differences (parameterisations, numerical mixing and surface forcing  
515 products). Compared to the observations in Meinen and McPhaden (2001), the lower diabatic con-  
516 tribution may be caused by the fact that the 20°C isotherm is biased deep. A too deep isotherm in  
517 the eastern equatorial Pacific likely results in a lower contribution of the diabatic fluxes to changes  
518 in warm water volume, as these fluxes are strongest near the surface. However, the observational

519 estimates also include large uncertainties due to missing data (e.g. Meinen and McPhaden (2001)  
520 mention that their error bars are generally as large as their signal).

521 In the three strong El Niño events the timing and behaviour of the diabatic fluxes correspond  
522 well to the idealised simulation (compare Fig. 11b and Fig. 6c). One notable exception is that  
523 numerical mixing plays a somewhat larger role.

524 The diabatic fluxes during the 1988/89 and 2007/08 La Niña events also share a strong similarity  
525 with the idealised event (despite the symmetric nature of the idealised La Niña): strong surface  
526 forcing at the peak of the event increases WWV while at the same time its increase is compensated  
527 by a negative vertical mixing flux (blue shaded periods, Fig. 11b). During the 1988/89 event,  
528 mixing undergoes changes associated with positive and negative contributions that mostly cancel  
529 out over the full recharge period (light blue line, Fig. 11b). In July 1988, the 20°C isotherm is  
530 largely within the warming region of vertical mixing, effectively causing a net positive volume  
531 flux into the WWV (Fig. 12a). Six months later, as the isotherm outcrops in the far eastern  
532 equatorial Pacific, the cooling via mixing near the surface exceeds the warming further west where  
533 the isotherm is deeper (Fig. 12b). Finally, as the isotherm returns to its deeper position in May  
534 1989, it moves back into the region where mixing warms water masses (Fig. 12c). The results  
535 in Lengaigne et al. (2012) do not show these compensating fluxes throughout different phases of  
536 WWV recharge, possibly due to their low-pass temporal filter. During the strong La Niña event in  
537 2010/11, surface forcing exhibits a reduced amplitude compared to the previous La Niña events,  
538 and vertical mixing is increasing WWV. This behaviour of the diabatic fluxes is caused by the  
539 20°C isotherm being positioned much deeper than during the previous events in the region where  
540 vertical mixing warms waters.

541 The consistent behaviour of the diabatic fluxes during the three strong El Niño events is revealed  
542 when all three events are composited (Fig. 13a). The depletion of WWV by the diabatic fluxes

leads the peak of the event (i.e. the peak of the N34 index) by three to six months, similar to the idealised simulation (Fig. 6c). Vertical mixing in all three El Niño events increases from September the following year (i.e. month 20, Fig. 13a), indicating the shift to La Niña-like conditions after El Niño. During La Niña, the composite time series reveal the strong effect of surface forcing, mainly caused by the high amplitude during the 1988/89 event, and highlight the compensating stages of vertical mixing (Fig. 13c). While the behaviour of the diabatic fluxes is similar in strong and moderate El Niño events (although with a lower magnitude, not shown), moderate La Niña events do not show a strong surface forcing flux, but rather an increase in vertical mixing (Fig. 13e). These effects arise from the reduced upward shift of the 20°C isotherm, its prolonged position in the vertical mixing-warming (i.e. recharging) region, and the enhanced turbulence in the eastern equatorial Pacific.

#### *b. Second Phase: Adiabatic Fluxes*

The second phase of WWV changes during all discharge and recharge periods is linked to increased adiabatic transport across 5°N and 5°S, and is strongly in-phase with the overall changes in WWV (Fig. 13b, d). The positive transport anomalies before the peak of the event are consistent across the three strong El Niño events, as in the idealised simulation (red line, Fig. 13b). Peak adiabatic transport during El Niño events ranges between –22.2 to –18.2 Sv, and is about 25% larger than the transport during La Niña events (14.9 to 15.1 Sv). This highlights, as in the idealised simulations, the increased importance of the adiabatic fluxes during El Niño. The volume flux across 5°N during all three El Niño events in Fig. 11 is more dominant than the one across 5°S (not shown), agreeing with the studies of McGregor et al. (2013, 2014) and Zeller et al. (2019). This results from the interplay between the two EOF modes of wind stress anomalies and Ekman-induced surface transport (McGregor et al. 2014). The Indonesian Throughflow (green line, Fig.

566 11a) is opposing changes in the adiabatic transport across 5°N and 5°S during all ENSO events,  
567 caused by a reduced volume transport during El Niño and increased transport during La Niña as  
568 discussed above. The contributions of meridional transport and the ITF to changes in WWV over  
569 the 1982/83 and 1997/98 El Niño events (79% and 67%) are higher compared to the values for  
570 the same events (63% and 45%) in Lengaigne et al. (2012). The differences during these events,  
571 as well as during the 1988/89 La Niña, may arise from their 16 month–8 years low pass temporal  
572 filter reducing the contribution of meridional transport.

## 573 9. Conclusions

574 In this study, we analysed the diabatic and adiabatic volume fluxes and associated non-linear  
575 ocean processes that contribute to WWV variability during ENSO events. To this end, we con-  
576 structed idealised, symmetric ENSO-related atmospheric fields to force a global high-resolution  
577 ocean-sea ice model and compared these simulations with the event-to-event variability from a  
578 1979–2016 hindcast simulation. The use of the WMT framework made it possible to individually  
579 calculate all fluxes that contribute to changes in WWV.

580 Changes to the WWV during El Niño’s discharge were initiated by the diabatic volume fluxes  
581 associated with surface forcing and vertical mixing, both strongly linked to the 20°C isotherm  
582 position and the strength of the trade winds. Weaker trade winds during El Niño reduce upwelling  
583 of cold water moving the 20°C isotherm away from the surface while also increasing eastern  
584 equatorial SSTs and driving an anomalous surface heat flux into the atmosphere. This results in  
585 an anomalous decrease of WWV due to surface forcing (dark blue sections, Fig. 14a). At the  
586 same time, the deepening 20°C isotherm moves away from the region of strong wind- and shear-  
587 driven mixing, whose intensity also reduces (light blue sections, Fig. 14a). The second phase  
588 of WWV discharge, occurring about six months later, was controlled by meridional adiabatic

589 transport across 5°N and 5°S with the ITF always acting to oppose changes in WWV (red and  
590 green sections, Fig. 14a).

591 During La Niña, the stronger trade winds increase upwelling of cold water masses and the 20°C  
592 isotherm shoals, sometimes outcropping in the eastern Pacific. Exposure of the 20°C isotherm to  
593 increased heat uptake by surface forcing in this region creates a strong across-isotherm volume  
594 flux responsible for most of the WWV recharge (dark blue sections, Fig. 14b). While turbulence  
595 is enhanced during La Niña, the shoaling of the isotherm into the surface layers, where mixing  
596 drives cooling of water rather than warming, means that vertical mixing can drive an anomalous  
597 decrease in WWV (light blue sections, Fig. 14b). This key asymmetry, that mixing drives  
598 anomalous discharge in both El Niño and La Niña events, arises from the strong dependence of  
599 the diabatic fluxes on the position of the 20°C isotherm. However, in the hindcast simulation (as  
600 opposed to the idealised simulations) the contribution of vertical mixing to the overall discharge  
601 during La Niña is concealed by opposing volume fluxes occurring at different times as the 20°C  
602 isotherm transitions through regions of vertical mixing-driven warming and cooling. In contrast,  
603 the idealised simulations, which are forced with symmetric atmospheric forcing, highlight the key  
604 role of the diabatic fluxes in driving ocean-sourced asymmetries in the WWV budget. On average,  
605 the ratio of the diabatic to adiabatic contributions to WWV changes during El Niño is about 40%  
606 : 60% while for La Niña, this ratio changes to 75% : 25%.

607 While the diabatic fluxes in the observed WWV budget in Meinen and McPhaden (2001) could  
608 only be derived as the residual from the horizontal transport, the model study by Brown and Fe-  
609 dorov (2010) showed that errors in the calculation of horizontal fluxes can be of the same magni-  
610 tude as the vertical fluxes. They further present evidence that the vertical fluxes on ENSO-related  
611 time scales in the eastern Pacific are small, contradicting the observational studies by Meinen and  
612 McPhaden (2000, 2001) and the modelling study by Lengaigne et al. (2012). By revisiting the

WWV budget with a precise online calculation of the individual fluxes, we were able to further minimise errors associated with the closure of this budget and thereby highlight the dominant role of the diabatic fluxes during La Niña. Despite differences to Meinen and McPhaden (2000) and Lengaigne et al. (2012) in the methods used to calculate the WWV budget terms (limited observations vs. the use of different models, parameterisation schemes and atmospheric forcing) our study supports the main finding that diabatic volume fluxes are as important as adiabatic volume fluxes in driving WWV changes on ENSO time scales. Our results are at odds with the conclusions of Brown and Fedorov (2010). The differences may arise because their short 6-year simulation over 1992–98 does not capture a strong La Niña where diabatic fluxes play a larger role. They also define the WWV as the volume of water above the  $25 \text{ kg m}^{-3}$  isopycnal that is up to 25 m shallower than the  $20^\circ\text{C}$  isotherm in the EUC (see their Fig. 1b) and use a 30-day running mean for their diapycnal transport.

The results in this study highlight the key role of diabatic processes in the eastern equatorial Pacific on ENSO time scales. A good representation of diffusive mixing and turbulence in models is therefore needed in order to correctly simulate these processes. The large event-to-event variability of ENSO in the hindcast simulation motivates future research into the evolution, spatial extent and amplitude of different events. Furthermore, it will be of value to investigate the decadal to multidecadal variability of WWV and ocean heat content to gain insight into the role of the equatorial Pacific in long-term heat uptake and redistribution, especially in light of current climate change.

**Acknowledgments.** The authors are supported by the Australian Research Council, including the ARC Centre of Excellence for Climate Extremes, through grant FL150100090 and MHE is additionally supported by the Centre for Southern Hemisphere Oceans Research (CSHOR). We

636 thank P. Spence for the 500-year CORE-NYF spin-up of the model and A. Kiss for the 300-year  
 637 JRA55-do spin-up of the hindcast simulation. We thank I. Medhaug, R. Knutti, N. Maher and S.  
 638 McGregor for valuable discussions and input during this project. We also thank the two anonym-  
 639 ous reviewers for comments and suggestions that helped improve the quality of the paper. The  
 640 simulations in this project were conducted with resources and services from the National Computa-  
 641 tional Infrastructure which is supported by the Australian Government. We thank NOAA's GFDL,  
 642 ESRL, NODC and the TAO Project Office of NOAA/PMEL as well as the Japanese Meteorologi-  
 643 cal Agency for free access to their CORE-NYF, SST, WWV, World Ocean Atlas and the Japanese  
 644 Ocean Reanalysis data. We thank the ECMWF for providing free access to the complete ERA-  
 645 Interim and ORA-S5 products. We also thank the Consortium for Ocean-Sea Ice Modelling in  
 646 Australia (COSIMA; [www.cosima.org.au](http://www.cosima.org.au)) for their technical help, continued development and for  
 647 making the ACCESS-OM2 suite of models available at <https://github.com/COSIMA/access-om2>.  
 648 The model output is available upon request to the authors and the analysis scripts are publicly  
 649 available at [https://github.com/mauricehuguenin/enso\\_diabatic\\_fluxes](https://github.com/mauricehuguenin/enso_diabatic_fluxes).

## 650 APPENDIX

### 651 **Derivation of Atmospheric Forcing for the Idealised Model Simulations**

652 The regression analysis and the idealised time series in Section 2b provide the spatial evolution for  
 653 wind stress perturbations related to ENSO. The patterns of the atmospheric variables used in the  
 654 idealised model simulations are obtained by regressing the full 38-year-long N34 and PC2 time  
 655 series onto each ERA-Interim anomaly field, resulting in two spatial patterns for each variable  
 656 (Examples are shown in Fig. A1).

657 The time evolution for the total atmospheric forcing is then calculated by multiplying the  $X_1$  and  
 658  $X_2$  spatial patterns with their associated idealised time series and adding them to the CORE-NYF

659 climatological forcing:

$$\underbrace{F_{ideal.}(x,y,t)}_{forcing} = \overline{F(x,y,t)} + \underbrace{X_{1,F}(x,y) \cdot N34_{ideal.}(t)}_{climatology} + \underbrace{X_{2,F}(x,y) \cdot PC2_{ideal.}(t)}_{perturbation}, \quad (1)$$

660 where  $F_{ideal.}(x,y,t)$  is one of the six idealised forcing anomaly fields dependent on time,  $\overline{F(x,y,t)}$  is  
661 the base forcing field without any interannual variability from the CORE-NYF data set,  $X_{1,F}(x,y)$ ,  
662  $X_{2,F}(x,y)$  are the two regression patterns of a given field  $F$  derived from the ERA-Interim product  
663 (Fig. 1), and  $N34_{ideal.}(t)$  and  $PC2_{ideal.}(t)$  are the associated idealised time series (Fig. 2). Put  
664 most simply, the ENSO perturbation forcing fields are derived from regressions of the  $N34_{ideal.}(t)$   
665 and  $PC2_{ideal.}(t)$  time-series onto the respective atmospheric fields required to construct the bulk  
666 formulae for heat and freshwater forcing.

667 For the remaining two input variables (zonal and meridional wind speed) we use a different  
668 method to derive the symmetric fields. In the model, wind speed is converted to wind stress by the  
669 wind stress law (Fairall et al. 1996):

$$\vec{\tau} = (\tau_x, \tau_y) = \rho_a \cdot C_D \cdot \underbrace{\sqrt{u_{10}^2 + v_{10}^2}}_{U_{10}} \cdot (u_{10}, v_{10}), \quad (2)$$

670 where  $\vec{\tau}$  is the wind stress vector with its zonal ( $\tau_x$ ) and meridional ( $\tau_y$ ) components [ $\text{N m}^{-2}$ ],  $\rho_a$   
671 is the density of air at sea level ( $1.25 \text{ kg m}^{-3}$ ),  $C_D$  is the unitless drag coefficient,  $u_{10}$  and  $v_{10}$  are  
672 the zonal and meridional wind speeds [ $\text{m s}^{-1}$ ] and  $U_{10}$  is the wind speed magnitude [ $\text{m s}^{-1}$ ]. For  
673 the derivation of the atmospheric forcing, we use a constant drag coefficient of  $1.5 \times 10^{-3}$  (Kara  
674 et al. 2007) for simplicity. Differences relative to the wind speed-dependent drag coefficient are  
675 negligible.

676 Due to the quadratic dependence of this equation on wind speed, the resulting wind stress anomalies  
677 lie if given symmetric ENSO-related wind speed anomalies are asymmetric. As we aimed for

symmetric wind stress anomalies during our El Niño and La Niña simulations, we therefore solved this equation in an inverse manner for the two unknowns  $u_{10}$  and  $v_{10}$ . To solve Equation 2 for wind speed, we first obtained the wind stress anomaly fields  $\tau'_x$  and  $\tau'_y$  from the EOF analysis described in Section 2, i.e. from  $\tau'_x = X_{1,\tau'_x} \cdot N34_{ideal.} + X_{2,\tau'_x} \cdot PC2_{ideal.}$  for the zonal component during El Niño (Fig. 1a, b and Fig. 2). The following section sets out how we then used the wind stress law to solve for the two unknowns  $u_{10}$  and  $v_{10}$ .

First, the zonal component of the wind stress law is rewritten as a Reynolds decomposition:

$$\underbrace{\bar{\tau}_x + \tau'_x}_{l} = \underbrace{\rho_a \cdot C_D}_{k} \cdot \underbrace{\sqrt{(\bar{u}_{10} + u'_{10})^2 + (\bar{v}_{10} + v'_{10})^2}}_{U_{10}} \cdot (\bar{u}_{10} + u'_{10}) \quad (3)$$

$$\Rightarrow l = k \cdot U_{10} \cdot (\bar{u}_{10} + u'_{10}),$$

where  $\bar{u}_{10}$  and  $\bar{v}_{10}$  are the climatological values from the CORE-NYF data set,  $\bar{\tau}_x$  is calculated from  $\bar{u}_{10}$  and  $\bar{v}_{10}$  by Equation 2,  $\tau'_x$ ,  $u'_{10}$  and  $v'_{10}$  are the perturbation values,  $l$  is the total zonal wind stress forcing including climatological and perturbation values and  $k$  contains the two constants for the density of air and the drag coefficient. Solving the second line of Equation 3 for  $u'_{10}$  results in

$$u'_{10} = \frac{l}{k \cdot U_{10}} - \bar{u}_{10}. \quad (4)$$

The same procedure as in Equation 3 is applied to the meridional component and yields

$$v'_{10} = \frac{m}{k \cdot U_{10}} - \bar{v}_{10}, \quad (5)$$

where  $m = k \cdot U_{10} \cdot (\bar{v}_{10} + v'_{10})$  is the total meridional wind stress forcing including climatological and perturbation values.

As a next step we combine  $l$  and  $m$  resulting in the following expression:

$$l^2 + m^2 = k^2 \cdot U_{10}^2 \cdot [(\bar{u}_{10} + u'_{10})^2 + (\bar{v}_{10} + v'_{10})^2] \\ = k^2 \cdot U_{10}^4, \quad (6)$$

694 and solve for the positive wind speed magnitude  $U_{10}$ :

$$U_{10} = \left| \frac{\sqrt[4]{l^2 + m^2}}{\sqrt{k}} \right|. \quad (7)$$

695 Inserting Equation (7) into Equations 4 and 5 allows us to solve for the two unknowns  $u'_{10}$  and  $v'_{10}$ :

$$u'_{10} = \pm \frac{l \cdot \sqrt{k}}{k \cdot \sqrt[4]{l^2 + m^2}} - \bar{u}_{10}, \quad (8)$$

$$v'_{10} = \pm \frac{m \cdot \sqrt{k}}{k \cdot \sqrt[4]{l^2 + m^2}} - \bar{v}_{10}, \quad (9)$$

697 where the correct sign is determined using the wind stress anomaly spatial patterns.

698 By using this approach, it is ensured that desired symmetric wind stress anomalies are applied to  
699 the model. However, wind speed values from Equation 8 and Equation 9 are also used to calculate  
700 the wind speed magnitude in the bulk formulae of sensible and latent heat fluxes (Equations 2a,  
701 b and Equation 3 in Fairall et al. 1996). Using the asymmetric wind speed values thus leads to  
702 asymmetric sensible and latent heat fluxes and furthermore also results in an 18% higher mean  
703 wind speed magnitude during La Niña than El Niño. While this asymmetry in sensible and latent  
704 heat fluxes as well as in wind speed magnitude is not ideal, it is of less importance than applying  
705 the correct symmetric wind stress values.

## 706 References

- 707 Bernie, D. J., S. J. Woolnough, J. M. Slingo, and E. Guilyardi, 2005: Modeling diurnal and in-  
708 traseasonal variability of the ocean mixed layer. *Journal of Climate*, **18** (8), 1190–1202, doi:  
709 10.1175/JCLI3319.1.
- 710 Bosc, C., and T. Delcroix, 2008: Observed equatorial Rossby waves and ENSO-related warm wa-  
711 ter volume changes in the equatorial Pacific Ocean. *Journal of Geophysical Research: Oceans*,  
712 **113** (C6), doi:10.1029/2007JC004613.

- 713 Brown, J. N., and A. V. Fedorov, 2010: Estimating the Diapycnal Transport Contribution to Warm  
714 Water Volume Variations in the Tropical Pacific Ocean. *Journal of Climate*, **23** (2), 221–237,  
715 doi:10.1175/2009JCLI2347.1.
- 716 Burgers, G., F.-F. Jin, and G. J. van Oldenborgh, 2005: The simplest ENSO recharge oscillator.  
717 *Geophysical Research Letters*, **32** (13), doi:10.1029/2005GL022951.
- 718 Cheng, L., K. E. Trenberth, J. T. Fasullo, M. Mayer, M. Balmaseda, and J. Zhu, 2019: Evolution  
719 of Ocean Heat Content Related to ENSO. *Journal of Climate*, **32** (12), 3529–3556, doi:10.1175/  
720 JCLI-D-18-0607.1.
- 721 Clarke, A. J., S. Van Gorder, and G. Colantuono, 2007: Wind Stress Curl and ENSO Dis-  
722 charge/Recharge in the Equatorial Pacific. *Journal of Physical Oceanography*, **37** (4), 1077–  
723 1091, doi:10.1175/JPO3035.1.
- 724 Colella, P., and P. R. Woodward, 1984: The Piecewise Parabolic Method (PPM) for gas-dynamical  
725 simulations. *Journal of Computational Physics*, **54** (1), 174–201, doi:10.1016/0021-9991(84)  
726 90143-8.
- 727 Collins, M., and Coauthors, 2010: The impact of global warming on the tropical Pacific Ocean  
728 and El Niño. *Nature Geoscience*, **3** (6), 391, doi:10.1038/ngeo868.
- 729 Dee, D., and Coauthors, 2011: The ERA-Interim reanalysis: Configuration and performance of  
730 the data assimilation system. *Quarterly Journal of the Royal Meteorological Society*, **137** (656),  
731 553–597, doi:10.1002/qj.828.
- 732 Delworth, T. L., and Coauthors, 2012: Simulated Climate and Climate Change in the GFDL  
733 CM2.5 High-Resolution Coupled Climate Model. *Journal of Climate*, **25** (8), 2755–2781, doi:  
734 10.1175/JCLI-D-11-00316.1.

- 735 Diaz, H. F., M. P. Hoerling, and J. K. Eischeid, 2001: ENSO variability, teleconnections and  
736 climate change. *International Journal of Climatology*, **21** (15), 1845–1862, doi:10.1002/joc.  
737 631.
- 738 Fairall, C. W., E. F. Bradley, D. P. Rogers, J. B. Edson, and G. S. Young, 1996: Bulk param-  
739 eterization of air-sea fluxes for tropical ocean-global atmosphere coupled-ocean atmosphere  
740 response experiment. *Journal of Geophysical Research: Oceans*, **101** (C2), 3747–3764, doi:  
741 10.1029/95JC03205.
- 742 Feng, M., N. Zhang, Q. Liu, and S. Wijffels, 2018: The Indonesian throughflow, its variability and  
743 centennial change. *Geoscience Letters*, **5**, 3, doi:10.1186/s40562-018-0102-2.
- 744 Fox-Kemper, B., R. Ferrari, and R. Hallberg, 2008: Parameterization of mixed layer ed-  
745 dies. Part I: Theory and diagnosis. *Journal of Physical Oceanography*, **38**, 1145–1165, doi:  
746 10.1175/2007JPO3792.1.
- 747 Gent, P. R., and J. C. McWilliams, 1990: Isopycnal Mixing in Ocean Circulation Models.  
748 *Journal of Physical Oceanography*, **20** (1), 150–155, doi:10.1175/1520-0485(1990)020<0150:  
749 IMIOCM>2.0.CO;2.
- 750 Gregg, M. C., H. Peters, J. C. Wesson, N. S. Oakey, and T. J. Shay, 1985: Intensive measurements  
751 of turbulence and shear in the equatorial undercurrent. *Nature*, **318**, 140, doi:10.1038/318140a0.
- 752 Griffies, S. M., 2012: Elements of the modular ocean model (MOM). *GFDL Ocean Group Tech.*  
753 *Rep*, **7**, 620.
- 754 Groeskamp, S., S. M. Griffies, D. Iudicone, R. Marsh, A. G. Nurser, and J. D. Zika, 2019: The  
755 water mass transformation framework for ocean physics and biogeochemistry. *Annual Review*  
756 *of Marine Science*, **11** (1), 271–305, doi:10.1146/annurev-marine-010318-095421.

- 757 Hallberg, R., 2013: Using a resolution function to regulate parameterizations of oceanic mesoscale  
758 eddy effects. *Ocean Modelling*, **72**, 92 – 103, doi:10.1016/j.ocemod.2013.08.007.
- 759 Hartmann, D. L., and Coauthors, 2013: Observations: atmosphere and surface. *Climate Change*  
760 *2013 the Physical Science Basis: Working Group I Contribution to the Fifth Assessment Report*  
761 *of the Intergovernmental Panel on Climate Change*, Cambridge University Press.
- 762 Holmes, R. M., and L. N. Thomas, 2015: The Modulation of Equatorial Turbulence by Tropical  
763 Instability Waves in a Regional Ocean Model. *Journal of Physical Oceanography*, **45** (4), 1155–  
764 1173, doi:10.1175/JPO-D-14-0209.1.
- 765 Holmes, R. M., J. D. Zika, and M. H. England, 2019a: Diathermal Heat Transport in a  
766 Global Ocean Model. *Journal of Physical Oceanography*, **49** (1), 141–161, doi:10.1175/  
767 JPO-D-18-0098.1.
- 768 Holmes, R. M., J. D. Zika, R. Ferrari, A. F. Thompson, E. R. Newsom, and M. H. England, 2019b:  
769 Atlantic Ocean Heat Transport Enabled by Indo-Pacific Heat Uptake and Mixing. *Geophysical*  
770 *Research Letters*, **46** (23), 13 939–13 949, doi:10.1029/2019GL085160.
- 771 Horel, J. D., 1982: On the annual cycle of the tropical Pacific atmosphere and ocean. *Monthly*  
772 *Weather Review*, **110** (12), 1863–1878, doi:10.1175/1520-0493(1982)110<1863:OTACOT>2.0.  
773 CO;2.
- 774 Izumo, T., M. Lengaigne, J. Vialard, I. Suresh, and Y. Planton, 2018: On the physical interpretation  
775 of the lead relation between Warm Water Volume and the El Niño Southern Oscillation. *Climate*  
776 *Dynamics*, 1–20, doi:10.1007/s00382-018-4313-1.

- 777 Jin, F.-F., 1997a: An equatorial ocean recharge paradigm for ENSO. Part I: Conceptual model.  
778 *Journal of the Atmospheric Sciences*, **54** (7), 811–829, doi:10.1175/1520-0469(1997)054<0830:  
779 AEORPF>2.0.CO;2.
- 780 Jin, F.-F., 1997b: An equatorial ocean recharge paradigm for ENSO. Part II: A stripped-down cou-  
781 pled model. *Journal of the Atmospheric Sciences*, **54**, 830–847, doi:10.1175/1520-0469(1997)  
782 054<0830:AEORPF>2.0.CO;2.
- 783 Jochum, M., G. Danabasoglu, M. Holland, Y.-O. Kwon, and W. G. Large, 2008: Ocean viscosity  
784 and climate. *Journal of Geophysical Research: Oceans*, **113** (C6), doi:10.1029/2007JC004515.
- 785 Johnson, G. C., and A. N. Birnbaum, 2017: As El Niño builds, Pacific Warm Pool expands, ocean  
786 gains more heat. *Geophysical Research Letters*, **44** (1), 438–445, doi:10.1002/2016GL071767.
- 787 Kara, A. B., A. J. Wallcraft, E. J. Metzger, H. E. Hurlburt, and C. W. Fairall, 2007: Wind stress  
788 drag coefficient over the global ocean. *Journal of Climate*, **20** (23), 5856–5864, doi:10.1175/  
789 2007JCLI1825.1.
- 790 Kiss, A. E., and Coauthors, 2020: ACCESS-OM2: A Global Ocean-Sea Ice Model at Three Res-  
791 olutions. *Geoscientific Model Development Discussions*, 1–58, doi:10.5194/gmd-13-401-2020.
- 792 Large, W. G., J. C. McWilliams, and S. C. Doney, 1994: Oceanic vertical mixing: A review  
793 and a model with a non-local boundary layer parameterization. *Reviews of Geophysics*, **32** (4),  
794 363–403, doi:10.1029/94rg01872.
- 795 Large, W. G., and A. G. Nurser, 2001: Chapter 5.1 Ocean surface water mass transformation.  
796 *Ocean Circulation and Climate*, International Geophysics, Vol. 77, Academic Press, 317–336,  
797 doi:10.1016/S0074-6142(01)80126-1.

798 Large, W. G., and S. G. Yeager, 2004: Diurnal to Decadal Global Forcing for Ocean and  
799 Sea-Ice Models: The Data Sets and Flux Climatologies. *NCAR Technical Note*, doi:10.5065/  
800 D6KK98Q6.

801 Lengaigne, M., U. Hausmann, G. Madec, C. Menkes, J. Vialard, and J.-M. Molines, 2012:  
802 Mechanisms controlling warm water volume interannual variations in the equatorial Pacific:  
803 Diabatic versus adiabatic processes. *Climate Dynamics*, **38** (5-6), 1031–1046, doi:10.1007/  
804 s00382-011-1051-z.

805 Lien, R.-C., D. R. Caldwell, M. C. Gregg, and J. N. Moum, 1995: Turbulence variability at the  
806 equator in the central Pacific at the beginning of the 1991—1993 El Niño. *Journal of Geophys-*  
807 *ical Research: Oceans*, **100** (C4), 6881–6898, doi:10.1029/94JC03312.

808 Liu, C., A. Köhl, Z. Liu, F. Wang, and D. Stammer, 2016: Deep-reaching thermocline mix-  
809 ing in the equatorial Pacific cold tongue. *Nature Communications*, **7**, 11576, doi:10.1038/  
810 ncomms11576.

811 Liu, W., and Coauthors, 2015: Extended Reconstructed Sea Surface Temperature Version 4  
812 (ERSST.v4): Part II. Parametric and Structural Uncertainty Estimations. *Journal of Climate*,  
813 **28** (3), 931–951, doi:10.1175/JCLI-D-14-00007.1.

814 Locarnini, R. A., and Coauthors, 2013: World Ocean Atlas 2013, Volume 1: Temperature. NOAA  
815 *Atlas NESDIS 73:40*, L. S, Ed., US Government Printing Office, Washington D.C., 40 pp.

816 McGregor, S., N. Ramesh, P. Spence, M. H. England, M. J. McPhaden, and A. Santoso, 2013:  
817 Meridional movement of wind anomalies during ENSO events and their role in event termina-  
818 tion. *Geophysical Research Letters*, **40** (4), 749–754, doi:10.1002/grl.50136.

- 819 McGregor, S., A. Sen Gupta, D. Dommeneget, T. Lee, M. J. McPhaden, and W. S. Kessler, 2017:  
820 Factors influencing the skill of synthesized satellite wind products in the tropical Pacific. *Journal*  
821 *of Geophysical Research: Oceans*, **122** (2), 1072–1089, doi:10.1002/2016JC012340.
- 822 McGregor, S., P. Spence, F. U. Schwarzkopf, M. H. England, A. Santoso, W. S. Kessler, A. Tim-  
823 mermann, and C. W. Böning, 2014: ENSO-driven interhemispheric Pacific mass transports.  
824 *Journal of Geophysical Research: Oceans*, **119** (9), 6221–6237, doi:10.1002/2014JC010286.
- 825 McGregor, S., A. Timmermann, F.-F. Jin, and W. S. Kessler, 2016: Charging El Niño with  
826 off-equatorial westerly wind events. *Climate Dynamics*, **47** (3), 1111–1125, doi:10.1007/  
827 s00382-015-2891-8.
- 828 McGregor, S., A. Timmermann, N. Schneider, M. F. Stuecker, and M. H. England, 2012:  
829 The Effect of the South Pacific Convergence Zone on the Termination of El Niño Events  
830 and the Meridional Asymmetry of ENSO. *Journal of Climate*, **25** (16), 5566–5586, doi:  
831 10.1175/JCLI-D-11-00332.1.
- 832 McPhaden, M. J., 2012: A 21st century shift in the relationship between ENSO SST and warm  
833 water volume anomalies. *Geophysical Research Letters*, **39** (9), doi:10.1029/2012GL051826.
- 834 Meehl, G. A., J. M. Arblaster, J. T. Fasullo, A. Hu, and K. E. Trenberth, 2011: Model-based  
835 evidence of deep-ocean heat uptake during surface-temperature hiatus periods. *Nature Climate  
836 Change*, **1**, 360, doi:10.1038/nclimate1229.
- 837 Meinen, C. S., and M. J. McPhaden, 2000: Observations of Warm Water Volume Changes in the  
838 Equatorial Pacific and their Relationship to El Niño and La Niña. *Journal of Climate*, **13** (20),  
839 3551–3559, doi:10.1175/1520-0442(2000)013<3551:OOWWVC>2.0.CO;2.

- 840 Meinen, C. S., and M. J. McPhaden, 2001: Interannual variability in warm water volume transports  
841 in the equatorial Pacific during 1993–99. *Journal of Physical Oceanography*, **31** (5), 1324–1345,  
842 doi:10.1175/1520-0485(2001)031<1324:IVIWWV>2.0.CO;2.
- 843 Meinen, C. S., M. J. McPhaden, and G. C. Johnson, 2001: Vertical velocities and transports in  
844 the equatorial Pacific during 1993–99. *Journal of physical oceanography*, **31** (11), 3230–3248,  
845 doi:10.1175/1520-0485(2001)031<3230:VVATIT>2.0.CO;2.
- 846 Menkes, C. E., M. Lengaigne, J. Vialard, M. Puy, P. Marchesiello, S. Cravatte, and G. Cambon,  
847 2014: About the role of Westerly Wind Events in the possible development of an El Niño in  
848 2014. *Geophysical Research Letters*, **41** (18), 6476–6483, doi:10.1002/2014GL061186.
- 849 Morice, C. P., J. J. Kennedy, N. A. Rayner, and P. D. Jones, 2012: Quantifying uncertainties  
850 in global and regional temperature change using an ensemble of observational estimates: The  
851 HadCRUT4 data set. *Journal of Geophysical Research: Atmospheres*, **117** (D8), doi:10.1029/  
852 2011JD017187.
- 853 Moum, J. N., A. Perlin, J. D. Nash, and M. J. McPhaden, 2013: Seasonal sea surface cooling  
854 in the equatorial Pacific cold tongue controlled by ocean mixing. *Nature*, **500** (7460), 64, doi:  
855 10.1038/nature12363.
- 856 Neske, S., and S. McGregor, 2018: Understanding the warm water volume precursor of ENSO  
857 events and its interdecadal variation. *Geophysical Research Letters*, **45** (3), 1577–1585, doi:  
858 10.1002/2017GL076439.
- 859 Okumura, Y. M., and C. Deser, 2010: Asymmetry in the duration of El Niño and La Niña. *Journal*  
860 *of Climate*, **23** (21), 5826–5843, doi:10.1175/2010JCLI3592.1.

861 Pham, H. T., W. D. Smyth, S. Sarkar, and J. N. Moum, 2017: Seasonality of deep cycle turbulence  
862 in the eastern equatorial Pacific. *Journal of Physical Oceanography*, **47** (9), 2189–2209, doi:  
863 10.1175/JPO-D-17-0008.1.

864 Rayner, N., D. E. Parker, E. Horton, C. Folland, L. Alexander, D. Rowell, E. Kent, and A. Kaplan,  
865 2003: Global analyses of sea surface temperature, sea ice, and night marine air temperature  
866 since the late nineteenth century. *Journal of Geophysical Research: Atmospheres*, **108** (D14),  
867 doi:10.1029/2002JD002670.

868 Redi, M. H., 1982: Oceanic Isopycnal Mixing by Coordinate Rotation. *Journal of Physical  
869 Oceanography*, **12** (10), 1154–1158, doi:10.1175/1520-0485(1982)012<1154:OIMBCR>2.0.  
870 CO;2.

871 Reynolds, R. W., T. M. Smith, C. Liu, D. B. Chelton, K. S. Casey, and M. G. Schlax, 2007:  
872 Daily high-resolution-blended analyses for sea surface temperature. *Journal of Climate*, **20** (22),  
873 5473–5496, doi:10.1175/2007JCLI1824.1.

874 Roemmich, D., and J. Gilson, 2011: The global ocean imprint of ENSO. *Geophysical Research  
875 Letters*, **38** (13), doi:10.1029/2011GL047992.

876 Schott, F. A., J. P. McCreary Jr, and G. C. Johnson, 2004: Shallow overturning circulations of the  
877 tropical-subtropical oceans. *Earth's Climate*, **147**, 261–304, doi:10.1029/147GM15.

878 Shinoda, T., W. Han, E. J. Metzger, and H. E. Hurlburt, 2012: Seasonal variation of the Indonesian  
879 Throughflow in Makassar Strait. *Journal of Physical Oceanography*, **42** (7), 1099–1123, doi:  
880 10.1175/JPO-D-11-0120.1.

881 Smith, T. M., and R. W. Reynolds, 2003: Extended reconstruction of global sea surface tem-  
882 peratures based on COADS data (1854–1997). *Journal of Climate*, **16** (10), 1495–1510, doi:  
883 10.1175/1520-0442-16.10.1495.

884 Smyth, W. D., and J. N. Moum, 2013: Marginal instability and deep cycle turbulence in the  
885 eastern equatorial Pacific Ocean. *Geophysical Research Letters*, **40** (23), 6181–6185, doi:10.  
886 1002/2013GL058403.

887 Spence, P., R. M. Holmes, A. M. Hogg, S. M. Griffies, K. D. Stewart, and M. H. England, 2017:  
888 Localized rapid warming of West Antarctic subsurface waters by remote winds. *Nature Climate  
889 Change*, **7** (8), 595, doi:10.1038/nclimate3335.

890 Sprintall, J., and A. Révelard, 2014: The Indonesian Throughflow response to Indo-Pacific  
891 climate variability. *Journal of Geophysical Research: Oceans*, **119** (2), 1161–1175, doi:  
892 10.1002/2013JC009533.

893 Stewart, K., A. M. Hogg, S. Griffies, A. Heerdegen, M. Ward, P. Spence, and M. England, 2017:  
894 Vertical resolution of baroclinic modes in global ocean models. *Ocean Modelling*, **113**, 50–65,  
895 doi:10.1016/j.ocemod.2017.03.012.

896 Stuecker, M. F., F.-F. Jin, A. Timmermann, and S. McGregor, 2015: Combination Mode Dynamics  
897 of the Anomalous Northwest Pacific Anticyclone. *Journal of Climate*, **28** (3), 1093–1111, doi:  
898 10.1038/ngeo1826.

899 Stuecker, M. F., A. Timmermann, F.-F. Jin, S. McGregor, and H.-L. Ren, 2013: A combination  
900 mode of the annual cycle and the El Niño/Southern Oscillation. *Nature Geoscience*, **6** (7), 540,  
901 doi:10.1175/JCLI-D-14-00225.1.

- 902 Suarez, M. J., and P. S. Schopf, 1988: A Delayed Action Oscillator for ENSO. *Journal of the At-*  
903 *mospheric Sciences*, **45** (21), 3283–3287, doi:10.1175/1520-0469(1988)045<3283:ADAOFE>2.  
904 0.CO;2.
- 905 Timmermann, A., and Coauthors, 2018: El Niño–Southern Oscillation complexity. *Nature*,  
906 **559** (7715), 535–545, doi:10.1038/s41586-018-0252-6.
- 907 Trenberth, K., and Coauthors, 2007: Observations: surface and atmospheric climate change. Chapter  
908 3. *Climate change*, 235–336.
- 909 Trenberth, K. E., J. M. Caron, D. P. Stepaniak, and S. Worley, 2002: Evolution of El Niño—  
910 Southern Oscillation and global atmospheric surface temperatures. *Journal of Geophysical Re-*  
911 *search: Atmospheres*, **107** (D8), AAC 5–1–AAC 5–17, doi:10.1029/2000JD000298.
- 912 Tsujino, H., and Coauthors, 2018: JRA-55 based surface dataset for driving ocean–sea-ice models  
913 (JRA55-do). *Ocean Modelling*, **130**, 79–139, doi:10.1016/j.ocemod.2018.07.002.
- 914 Walin, G., 1982: On the relation between sea-surface heat flow and thermal circulation in the  
915 ocean. *Tellus*, **34** (2), 187–195, doi:10.3402/tellusa.v34i2.10801.
- 916 Warner, S. J., and J. N. Moum, 2019: Feedback of Mixing to ENSO Phase Change. *Geophysical*  
917 *Research Letters*, **46** (23), 13 920–13 927, doi:10.1029/2019GL085415.
- 918 Wu, Q., X. Zhang, J. A. Church, and J. Hu, 2019: ENSO-Related Global Ocean Heat Content  
919 Variations. *Journal of Climate*, **32** (1), 45–68, doi:10.1175/JCLI-D-17-0861.1.
- 920 Wyrtki, K., 1975: El Niño—The Dynamic Response of the Equatorial Pacific Ocean to  
921 Atmospheric Forcing. *Journal of Physical Oceanography*, **5** (4), 572–584, doi:10.1175/  
922 1520-0485(1975)005<0572:ENTDRO>2.0.CO;2.

- 923 Wyrtki, K., 1985: Water displacements in the Pacific and the genesis of El Nino cycles. *Journal of*  
924 *Geophysical Research: Oceans*, **90** (C4), 7129–7132, doi:10.1029/JC090iC04p07129.
- 925 Zeller, M., S. McGregor, and P. Spence, 2019: Hemispheric Asymmetry of the Pacific Shallow  
926 Meridional Overturning Circulation. *Journal of Geophysical Research: Oceans*, **124** (8), 5765–  
927 5786, doi:10.1029/2018JC014840.
- 928 Zuo, H., M. Balmaseda, K. Mogensen, and S. Tietsche, 2018: *OCEAN5: the ECMWF Ocean*  
929 *Reanalysis System and its Real-Time analysis component*. European Centre for Medium-Range  
930 Weather Forecasts.

## 931 LIST OF FIGURES

- 932 **Fig. 1.** The (a) first and (b) second mode of wind stress variability related to ENSO from the ERA-  
 933 Interim product [ $10^{-2}$  N m $^{-2}$ ]. The zonal wind stress component is shaded. The Niño-3.4  
 934 area ( $170^{\circ}\text{W}$ – $120^{\circ}\text{W}$  and  $5^{\circ}\text{N}$ – $5^{\circ}\text{S}$ ) is indicated as the framed area in (a). (c) The associated  
 935 time series with the observed N34 (Reynolds et al. 2007) in black and PC2 in red. The red  
 936 and blue shaded areas in (c) indicate the three strongest El Niño and La Niña events, each  
 937 covering a 24-month period centered around the peak N34 anomalies. . . . . 46
- 938 **Fig. 2.** The idealised synthetic time series in bold for N34 (black) and PC2 (red) during the two-  
 939 year-long El Niño event followed by a two-year-long spin-down period. The thin lines show the observed N34 values (black) and the calculated PC2 time series (red) during the  
 940 three strongest El Niño events in Fig. 1c, namely 1982–1983, 1997–1998 and 2014–2016,  
 941 centered in December. . . . . 47
- 942 **Fig. 3.** Anomalous time series for the (a, b) global mean sea surface temperature (GMSSST) [°C] and  
 943 globally integrated ocean heat content (OHC) [J] as well as (c, d) the idealised N34 index, the  
 944 simulated N34 index [°C] and the WWV anomalies [m $^3$ ] during the idealised and symmetric  
 945 El Niño and La Niña events. In (c) the correlation coefficient ( $r$ ) between the observed and  
 946 simulated N34 index is shown in blue. The vertical lines at months 24 represent the end of  
 947 the event and the subsequent start of the two-year-long spin-down period with climatological  
 948 forcing. . . . . 48
- 949 **Fig. 4.** Depth-longitude transects across the equatorial Pacific of the water mass transformation  
 950 velocities (Equations 3 and 2) for (a, c) vertical mixing  $\mathcal{G}_M$  and (b, d) surface forcing  $\mathcal{G}_F$   
 951 [ $\text{m day}^{-1}$ ] in the CORE-NYF control simulation. The WMT velocities are accumulated in  
 952 temperature space and remapped to depth using the mean isotherm depths. The upper two  
 953 panels show the annual mean and the lower panels the mean over the September–November  
 954 (SON) period when the diabatic fluxes are seasonally intense (Fig. 5b). The contours show  
 955 the distribution of the equatorial isotherms with the  $20^{\circ}\text{C}$  isotherm in bold. The dashed blue  
 956 line in the upper-most layers indicates the mixed layer depth defined as a  $0.032 \text{ kg m}^{-3}$   
 957 density difference from the surface. The discontinuity at  $90^{\circ}\text{W}$  is caused by the model's  
 958 bathymetry near the Galápagos Islands. . . . . 49
- 959 **Fig. 5.** Annual cycle of the climatological (a) adiabatic and (b) diabatic WWV budget terms [Sv  
 960  $\equiv 10^6 \text{ m}^3 \text{ s}^{-1}$ ] in the CORE-NYF control simulation. The change in WWV as the sum of  
 961 the other fluxes is shown as the black line in (a). Positive values indicate a volume flux  
 962 into the WWV region (i.e. a recharge) and negative values indicate a volume flux out of the  
 963 region (i.e. a discharge). A 3-month running mean has been applied. . . . . 50
- 964 **Fig. 6.** The (a, b) adiabatic and (c, d) diabatic WWV budget terms [Sv] as anomalies throughout  
 965 the idealised, symmetric El Niño and La Niña simulations. A five-month running mean as  
 966 in Meinen and McPhaden (2000) has been applied. The discharge phase (red shaded period  
 967 in panel a) is defined as the period when the change in WWV is negative from months 7–21.  
 968 To ensure a symmetric analysis during La Niña, the recharge phase (blue shaded period)  
 969 covers the same period. Positive values indicate volume transport into the WWV region (i.e.  
 970 a recharge), negative values represent transport out of the WWV region (i.e. a discharge). . . . . 51
- 971 **Fig. 7.** Mean depth-longitude transects for September–November across the equatorial Pacific of  
 972 the water mass transformation velocities for (a, c) vertical mixing  $\mathcal{G}_M$  and (b, d) surface  
 973 forcing  $\mathcal{G}_F$  [ $\text{m day}^{-1}$ ] during the idealised, symmetric El Niño and La Niña events. The  
 974 contours show the distribution of the equatorial isotherms with the  $20^{\circ}\text{C}$  isotherm in bold.  
 975

52

**Fig. 8.** Snapshots of the warm water volume during the peak of the idealised, symmetric (a) El Nio discharge and (b) La Nia recharge phases alongside the time-integrated contribution of the WWV budget terms over the full discharge/recharge period. The solid line between 116E–80W displays the climatological 20C isotherm depth and the dashed line its anomalous position during the event. Before the El Nio event, WWV is anomalously large (hence a deep isotherm) and the integrated WWV budget terms over the event result in the net discharge of WWV. The blue and red shaded areas in the eastern equatorial Pacific indicate where vertical mixing is cooling and warming water masses that lead to buoyancy-driven vertical heat and volume fluxes across isotherms indicated by the light blue arrows. The dark blue arrows show how anomalous surface forcing leads to (a) depletion and (b) build-up of WWV across the 20C isotherm. The two symbols  $\otimes$  and  $\odot$  illustrate meridional WWV transport out of and into the equatorial region respectively. Meridional transport here combines the horizontal transport across 5N, 5S and the ITF.

53

**Fig. 9.** Time series of the simulated N34 index [ $^{\circ}\text{C}$ ] and anomalous WWV [ $\text{m}^3$ ] during the 1979–2016 hindcast simulation compared to observations in Reynolds et al. (2007) and Meinen and McPhaden (2000). The observed indices are given as dashed blue and red lines and the correlation coefficients ( $r$ ) between the simulated and observed time series are indicated with blue and red values.

54

**Fig. 10.** Depth-longitude transect of the 20°C isotherm for September–November across the equatorial Pacific during the El Niño event in 1997 (blue lines) and La Niña event in 1998 (red lines) in the 1979–2016 hindcast simulation. The dashed blue and red lines show the isotherm distribution during the same time period in the ORA-S5 ocean reanalysis product (Zuo et al. 2018). In black the climatological position of the 20°C isotherm compared to the observations in the World Ocean Atlas (WOA13v2, Locarnini et al. 2013).

55

**Fig. 11.** (a) The change in the WWV anomaly as well as the adiabatic and (b) diabatic volume fluxes [Sv] during the 1979–2016 hindcast simulation. A five-month running mean as in Meinen and McPhaden (2000) has been applied. The red discharge and blue recharge periods for the three strongest El Niño and La Niña events are defined as when the rate of change in the WWV anomaly (black line in (a)) is negative and positive respectively. In (b) we also show the N34 index [ $^{\circ}\text{C}$ ] as a dashed black line and the total diabatic volume fluxes in grey. Positive and negative values indicate a contribution to the recharge and discharge of WWV respectively. 56

56

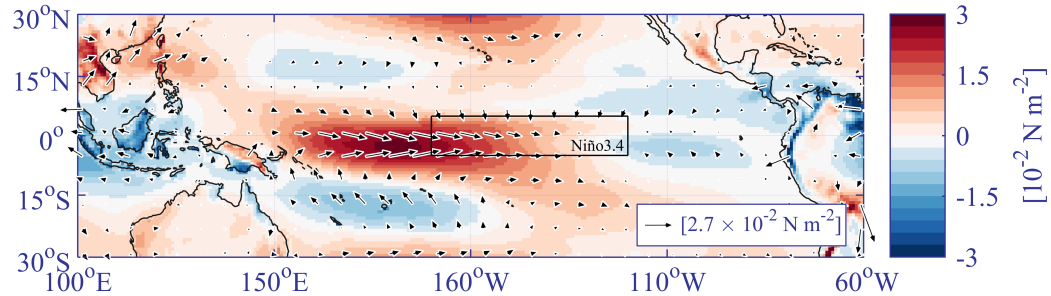
57

**Fig. 13.** Composite time series centered in December (month 12) of the (a, c) diabatic WWV budget terms as well as (b, d) the rate of change in WWV and the adiabatic terms [Sv] during the three strong El Niño and La Niña events shaded in red and blue in Fig. 11. The label 1988/89 in (c) shows the time series of the surface forcing term during the 1988/89 La Niña event.

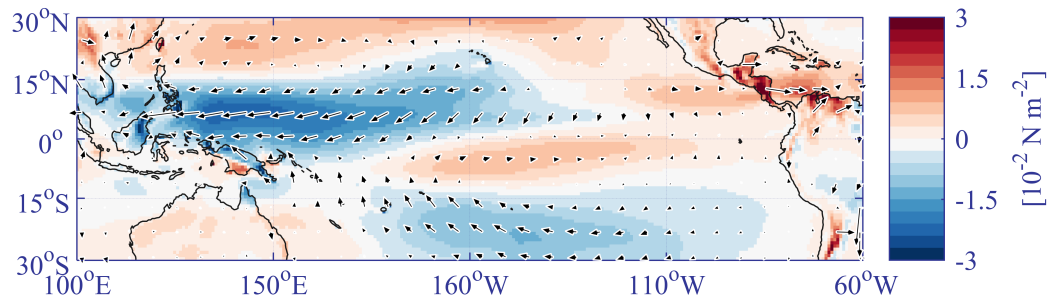
In (e) the composite diabatic time series for three moderate La Niña events in 1984/85, 1995/96, 2006/07. In the left panels we also show the time series for the N34 index [ $^{\circ}\text{C}$ ] (dashed black line). The faint lines are the time series corresponding to the three events while the solid lines are the composites.

**Fig. A1.** Examples of four out of the eight atmospheric regression patterns  $X_1$  associated with ENSO used in the atmospheric forcing for the idealised symmetric events. These spatial patterns are calculated by regressing the observed N34 index (Reynolds et al. 2007) onto anomalous spatial maps from the ERA-Interim reanalysis product for 1979–2016 (Dee et al. 2011) and taking the time mean. (a) Air temperature [ $^{\circ}\text{C}$ ], (b) specific humidity [ $\text{kg kg}^{-1}$ ], (c) downward short-wave radiation [ $\text{W m}^{-2}$ ] and (d) sea level pressure [Pa]. . . . . 60

a) First mode of wind stress variability  $X_{1,\tau}$  (58.6% variance)



b) Second mode of wind stress variability  $X_{2,\tau}$  (17.1% variance)



c) N34 and PC2 time series

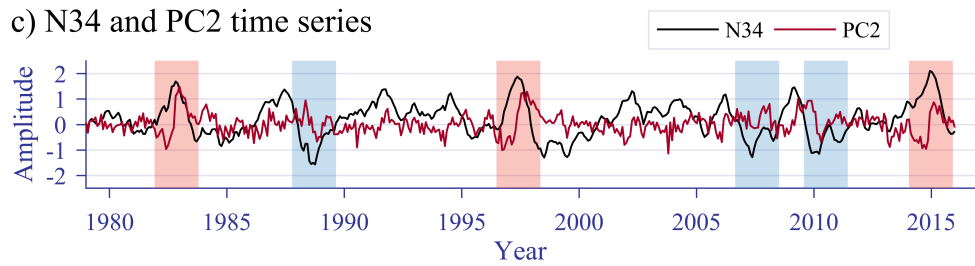
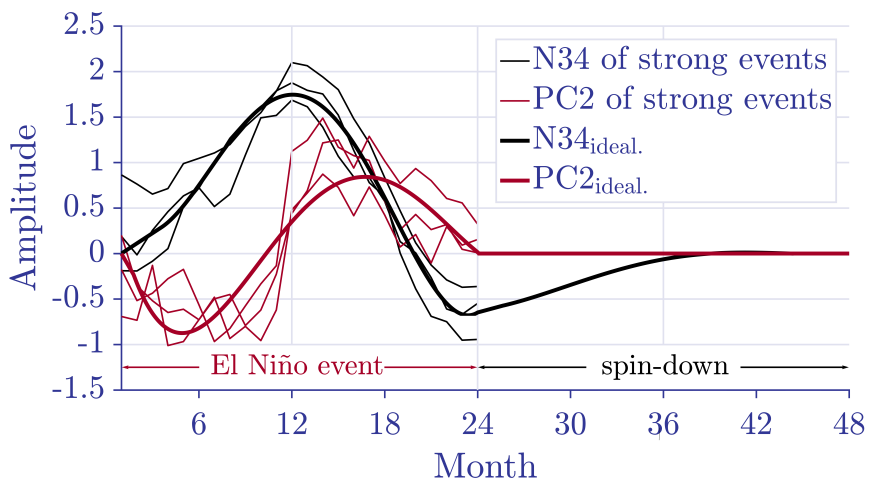


FIG. 1. The (a) first and (b) second mode of wind stress variability related to ENSO from the ERA-Interim product [ $10^{-2} \text{ N m}^{-2}$ ]. The zonal wind stress component is shaded. The Niño3.4 area ( $170^{\circ}\text{W}$ – $120^{\circ}\text{W}$  and  $5^{\circ}\text{N}$ – $5^{\circ}\text{S}$ ) is indicated as the framed area in (a). (c) The associated time series with the observed N34 (Reynolds et al. 2007) in black and PC2 in red. The red and blue shaded areas in (c) indicate the three strongest El Niño and La Niña events, each covering a 24-month period centered around the peak N34 anomalies.



1045 FIG. 2. The idealised synthetic time series in bold for N34 (black) and PC2 (red) during the two-year-long El  
1046 Niño event followed by a two-year-long spin-down period. The thin lines show the observed N34 values (black)  
1047 and the calculated PC2 time series (red) during the three strongest El Niño events in Fig. 1c, namely 1982–1983,  
1048 1997–1998 and 2014–2016, centered in December.

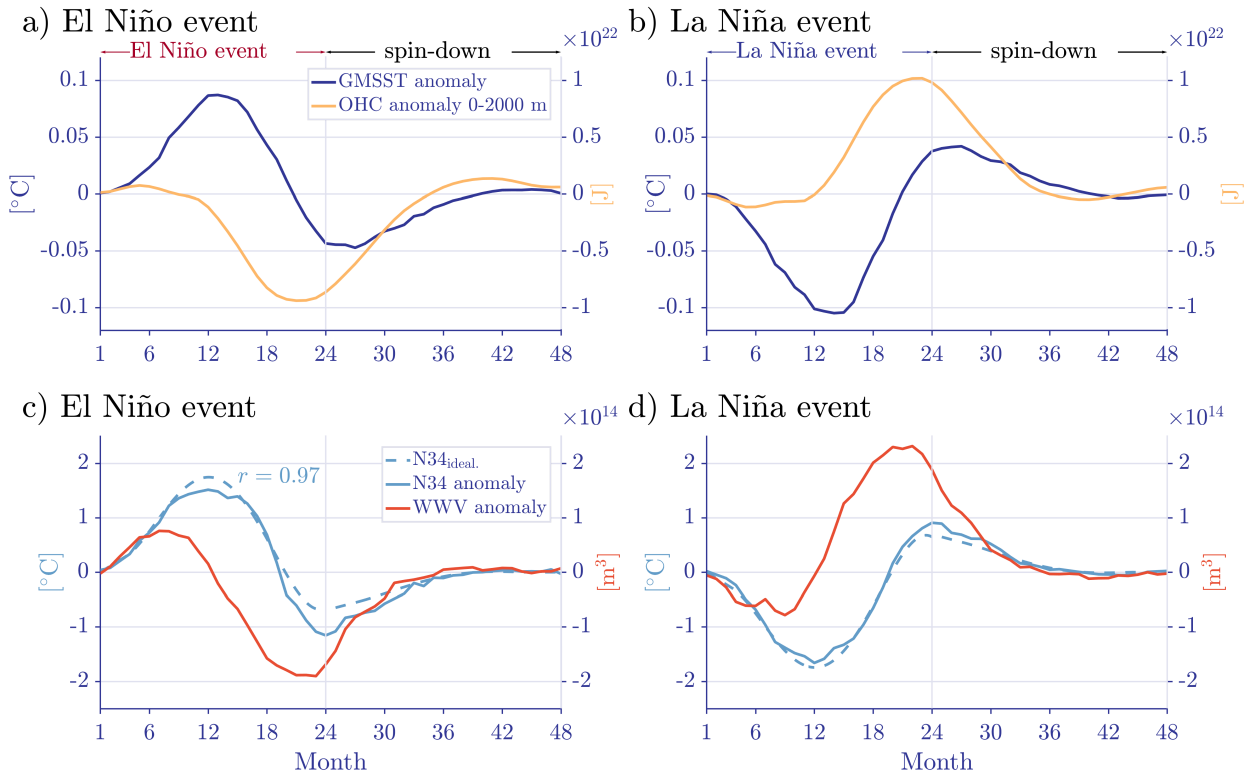


FIG. 3. Anomalous time series for the (a, b) global mean sea surface temperature (GMSST) [ $^{\circ}\text{C}$ ] and globally integrated ocean heat content (OHC) [J] as well as (c, d) the idealised N34 index, the simulated N34 index [ $^{\circ}\text{C}$ ] and the WWV anomalies [ $\text{m}^3$ ] during the idealised and symmetric El Niño and La Niña events. In (c) the correlation coefficient ( $r$ ) between the observed and simulated N34 index is shown in blue. The vertical lines at months 24 represent the end of the event and the subsequent start of the two-year-long spin-down period with climatological forcing.

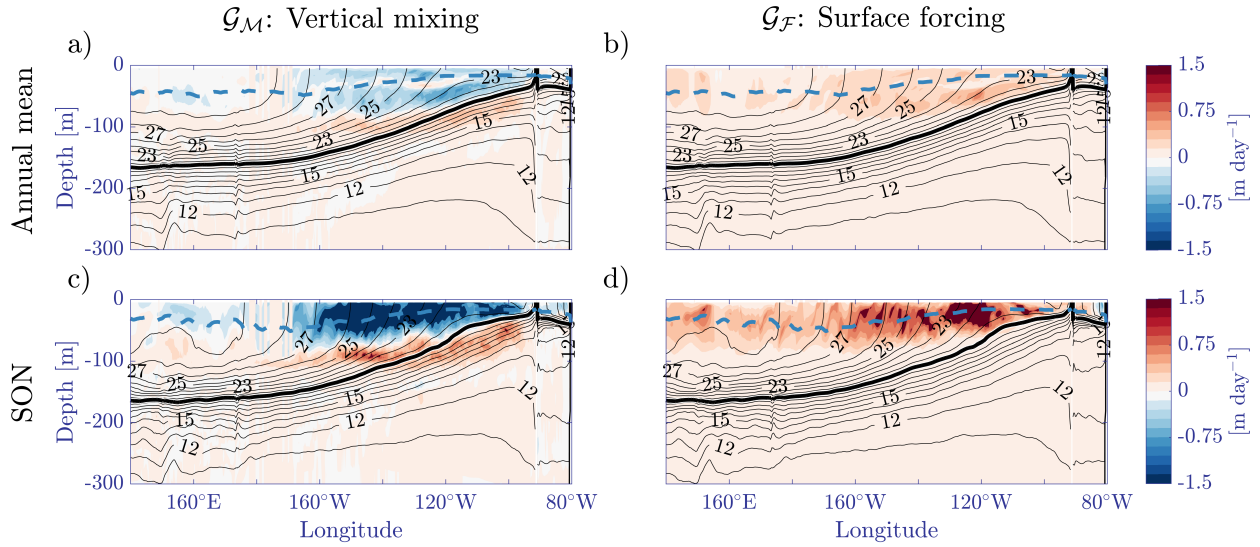


FIG. 4. Depth-longitude transects across the equatorial Pacific of the water mass transformation velocities (Equations 3 and 2) for (a, c) vertical mixing  $\mathcal{G}_M$  and (b, d) surface forcing  $\mathcal{G}_F$  [ $\text{m day}^{-1}$ ] in the CORE-NYF control simulation. The WMT velocities are accumulated in temperature space and remapped to depth using the mean isotherm depths. The upper two panels show the annual mean and the lower panels the mean over the September-November (SON) period when the diabatic fluxes are seasonally intense (Fig. 5b). The contours show the distribution of the equatorial isotherms with the  $20^\circ\text{C}$  isotherm in bold. The dashed blue line in the upper-most layers indicates the mixed layer depth defined as a  $0.032 \text{ kg m}^{-3}$  density difference from the surface. The discontinuity at  $90^\circ\text{W}$  is caused by the model's bathymetry near the Galápagos Islands.

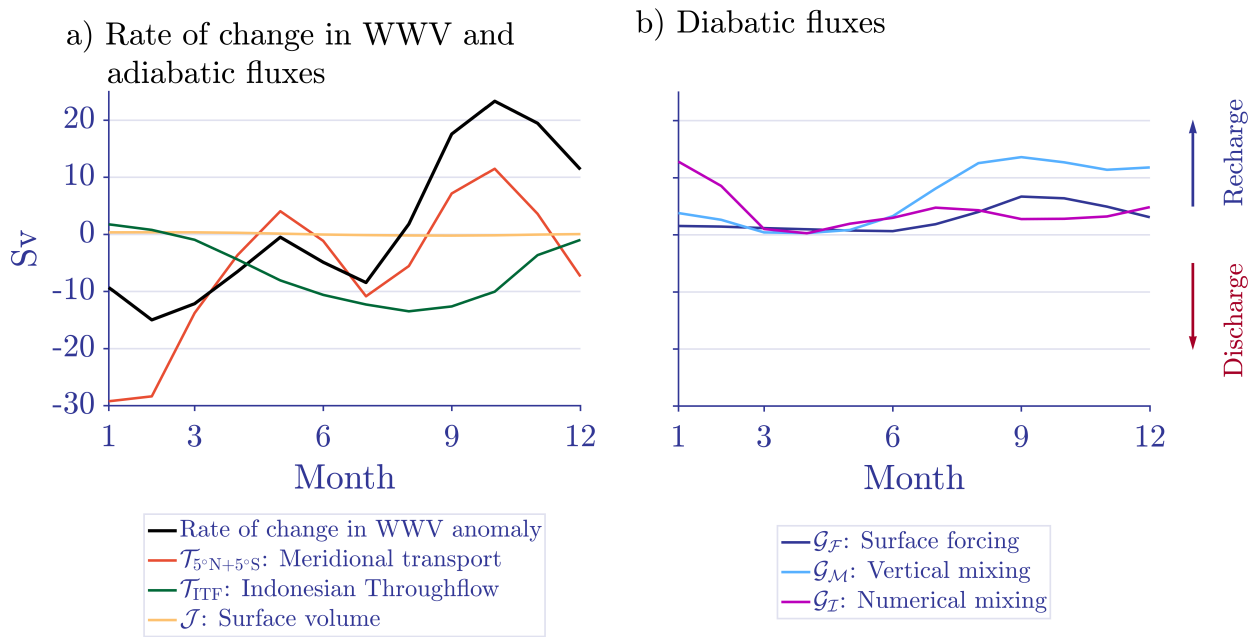


FIG. 5. Annual cycle of the climatological (a) adiabatic and (b) diabatic WWV budget terms [ $\text{Sv} \equiv 10^6 \text{ m}^3 \text{ s}^{-1}$ ] in the CORE-NYF control simulation. The change in WWV as the sum of the other fluxes is shown as the black line in (a). Positive values indicate a volume flux into the WWV region (i.e. a recharge) and negative values indicate a volume flux out of the region (i.e. a discharge). A 3-month running mean has been applied.

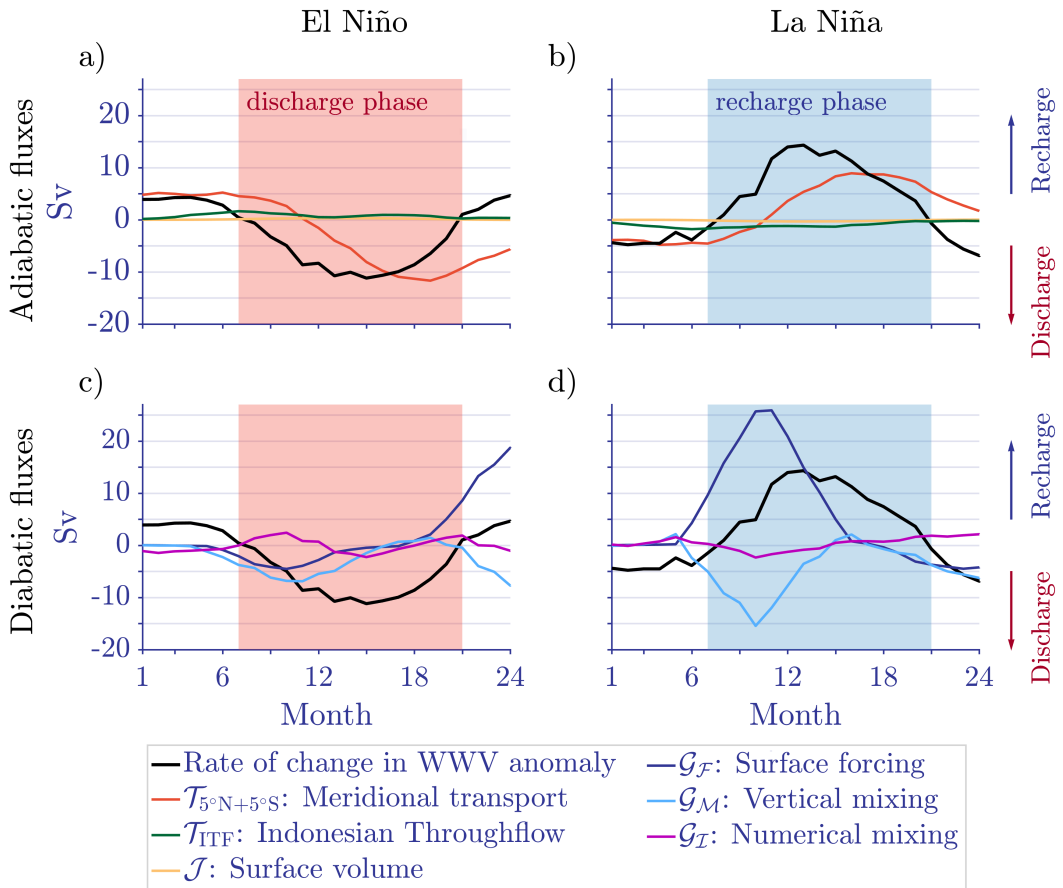
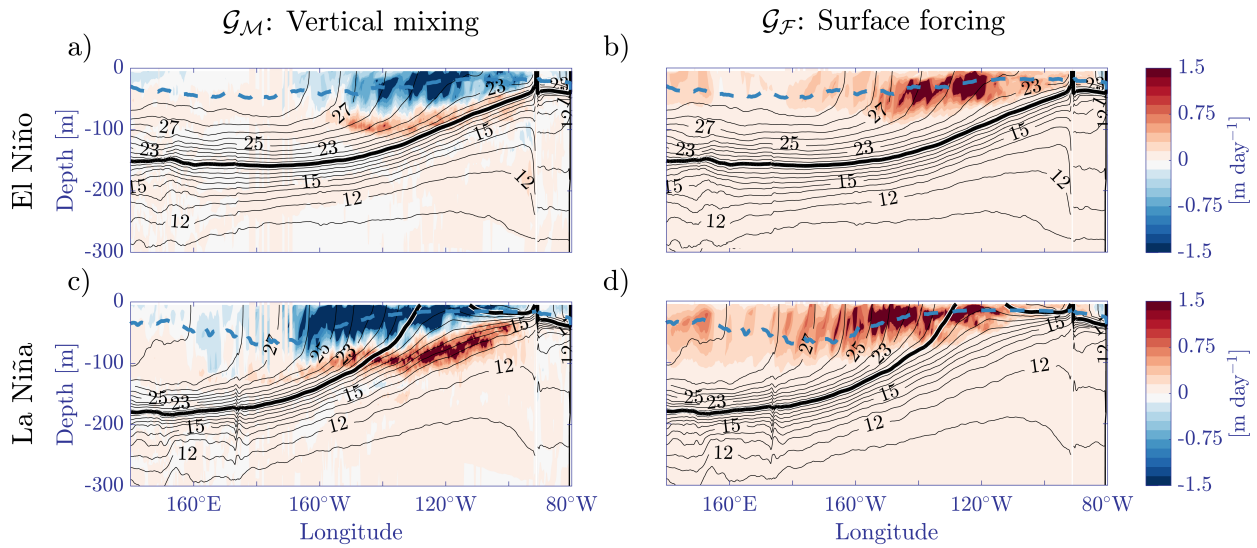


FIG. 6. The (a, b) adiabatic and (c, d) diabatic WWV budget terms [Sv] as anomalies throughout the idealised, symmetric El Niño and La Niña simulations. A five-month running mean as in Meinen and McPhaden (2000) has been applied. The discharge phase (red shaded period in panel a) is defined as the period when the change in WWV is negative from months 7–21. To ensure a symmetric analysis during La Niña, the recharge phase (blue shaded period) covers the same period. Positive values indicate volume transport into the WWV region (i.e. a recharge), negative values represent transport out of the WWV region (i.e. a discharge).



1073 FIG. 7. Mean depth-longitude transects for September-November across the equatorial Pacific of the water  
 1074 mass transformation velocities for (a, c) vertical mixing  $\mathcal{G}_M$  and (b, d) surface forcing  $\mathcal{G}_F$  [ $m \text{ day}^{-1}$ ] during the  
 1075 idealised, symmetric El Niño and La Niña events. The contours show the distribution of the equatorial isotherms  
 1076 with the  $20^\circ\text{C}$  isotherm in bold. The dashed blue line in the upper-most layers indicates the mixed layer depth  
 1077 as defined in Fig. 4.

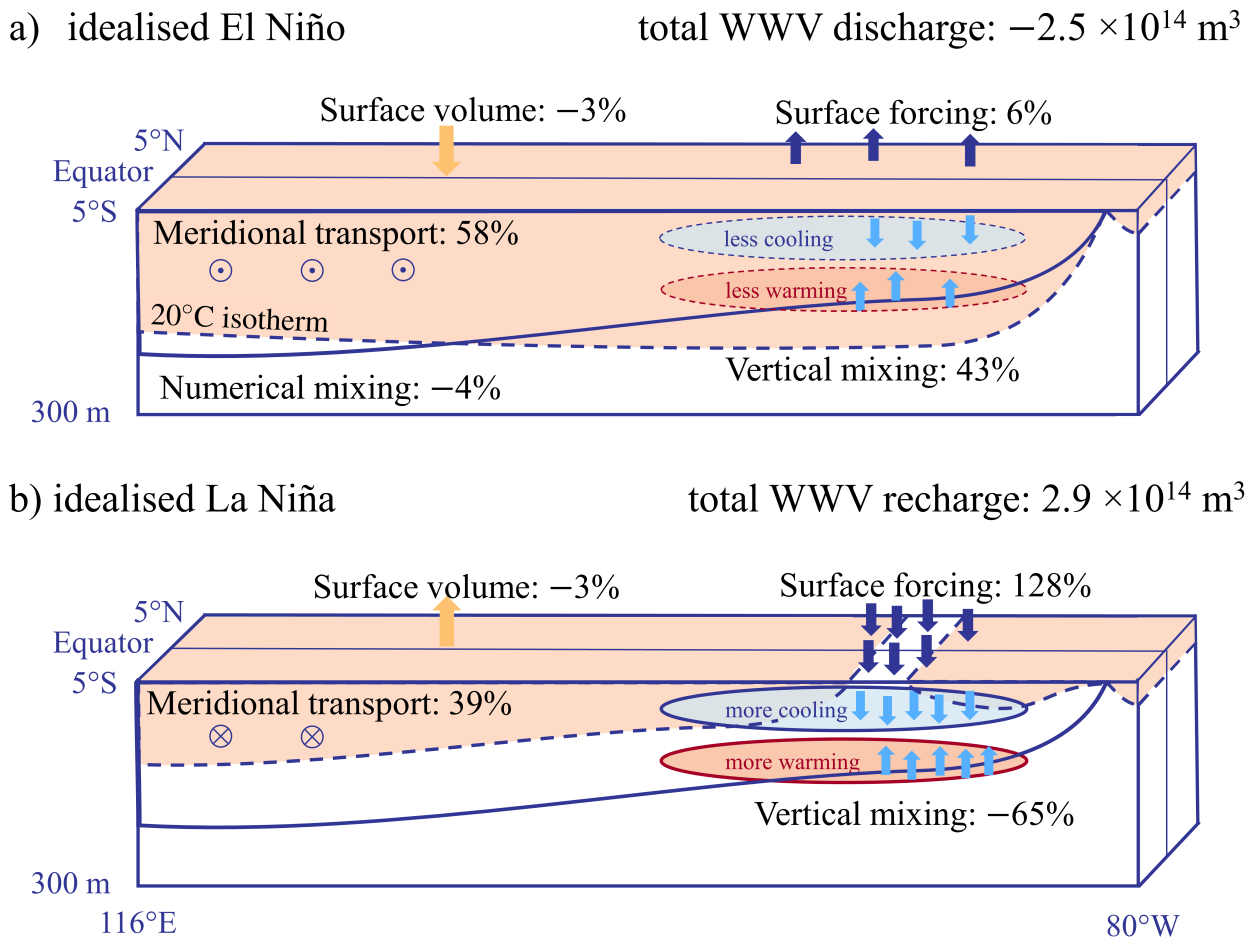


FIG. 8. Snapshots of the warm water volume during the peak of the idealised, symmetric (a) El Niño discharge and (b) La Niña recharge phases alongside the time-integrated contribution of the WWV budget terms over the full discharge/recharge period. The solid line between 116°E–80°W displays the climatological 20°C isotherm depth and the dashed line its anomalous position during the event. Before the El Niño event, WWV is anomalously large (hence a deep isotherm) and the integrated WWV budget terms over the event result in the net discharge of WWV. The blue and red shaded areas in the eastern equatorial Pacific indicate where vertical mixing is cooling and warming water masses that lead to buoyancy-driven vertical heat and volume fluxes across isotherms indicated by the light blue arrows. The dark blue arrows show how anomalous surface forcing leads to (a) depletion and (b) build-up of WWV across the 20°C isotherm. The two symbols  $\otimes$  and  $\odot$  illustrate meridional WWV transport out of and into the equatorial region respectively. Meridional transport here combines the horizontal transport across 5°N, 5°S and the ITF.

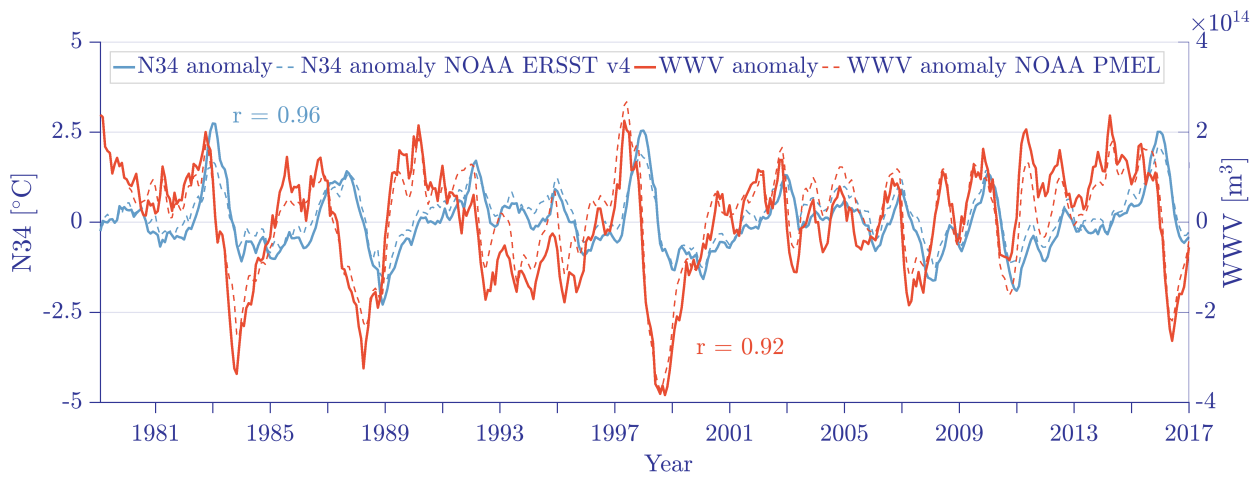


FIG. 9. Time series of the simulated N34 index [ $^{\circ}\text{C}$ ] and anomalous WWV [ $\text{m}^3$ ] during the 1979–2016 hindcast simulation compared to observations in Reynolds et al. (2007) and Meinen and McPhaden (2000). The observed indices are given as dashed blue and red lines and the correlation coefficients ( $r$ ) between the simulated and observed time series are indicated with blue and red values.

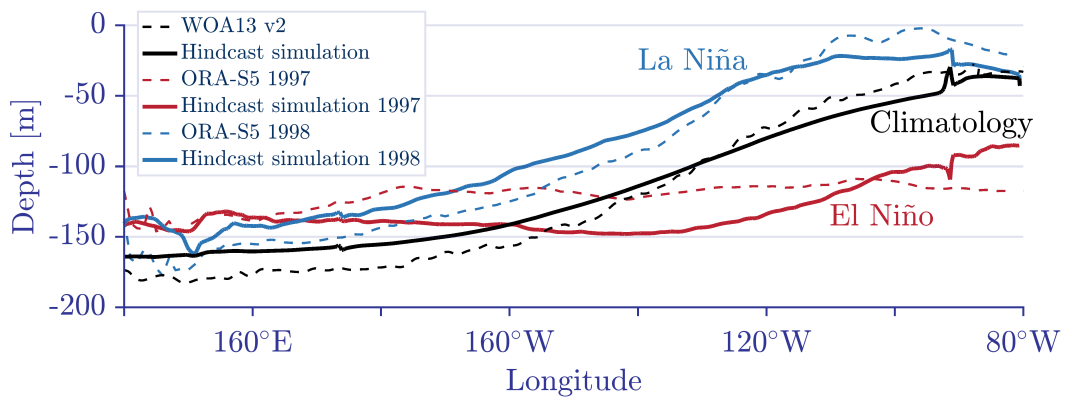


FIG. 10. Depth-longitude transect of the 20°C isotherm for September–November across the equatorial Pacific during the El Niño event in 1997 (blue lines) and La Niña event in 1998 (red lines) in the 1979–2016 hindcast simulation. The dashed blue and red lines show the isotherm distribution during the same time period in the ORA-S5 ocean reanalysis product (Zuo et al. 2018). In black the climatological position of the 20°C isotherm compared to the observations in the World Ocean Atlas (WOA13v2, Locarnini et al. 2013).

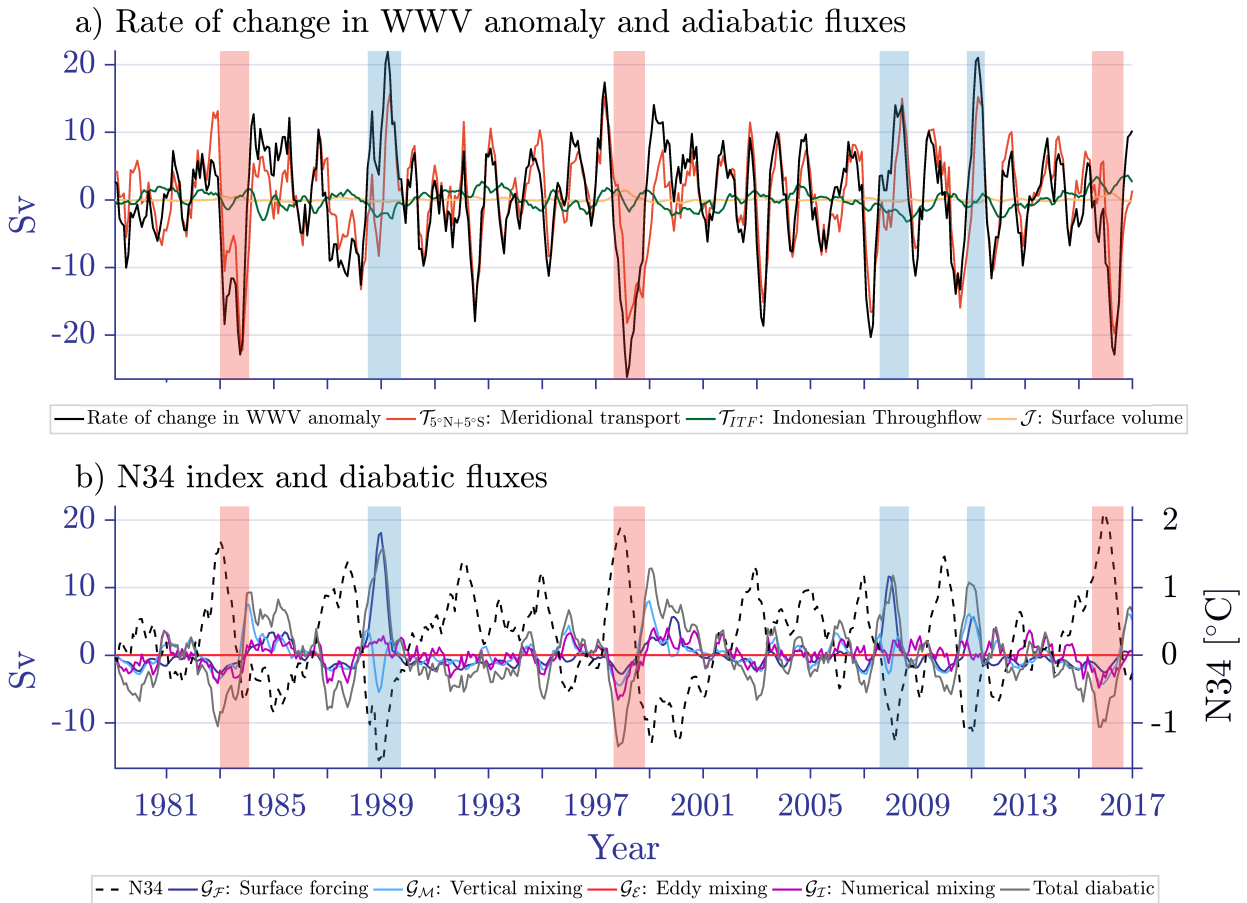
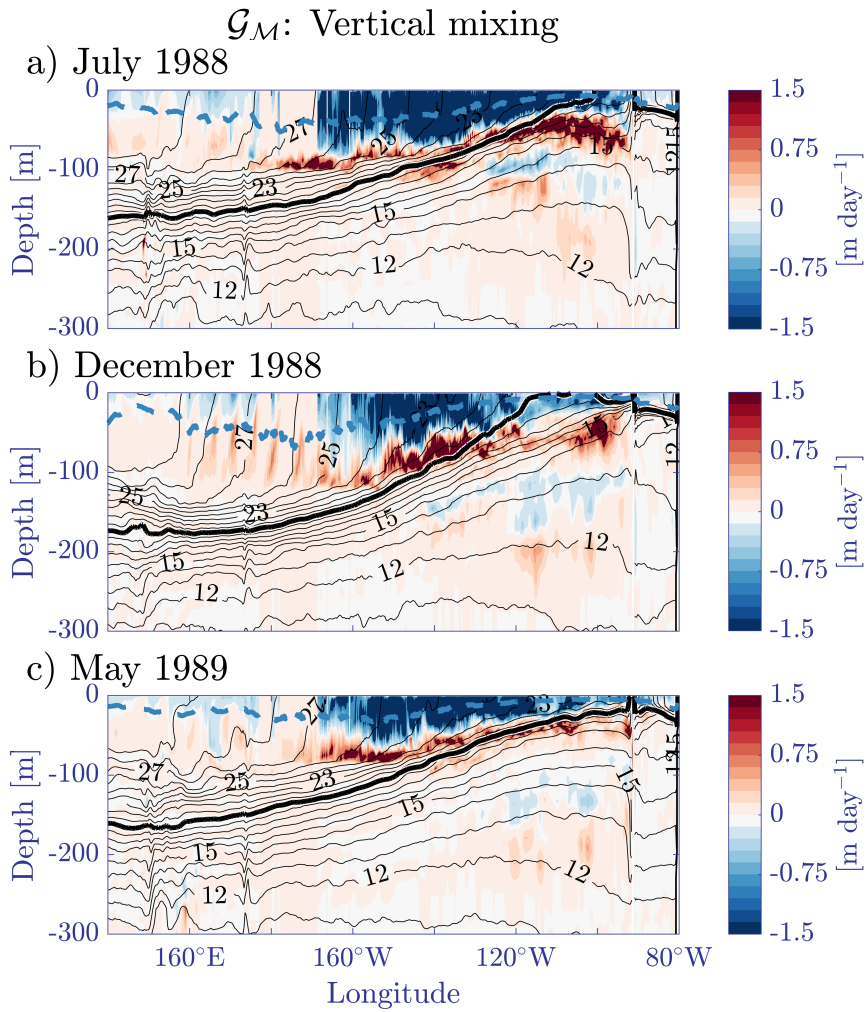


FIG. 11. (a) The change in the WWV anomaly as well as the adiabatic and (b) diabatic volume fluxes [Sv] during the 1979–2016 hindcast simulation. A five-month running mean as in Meinen and McPhaden (2000) has been applied. The red discharge and blue recharge periods for the three strongest El Niño and La Niña events are defined as when the rate of change in the WWV anomaly (black line in (a)) is negative and positive respectively. In (b) we also show the N34 index [ $^{\circ}\text{C}$ ] as a dashed black line and the total diabatic volume fluxes in grey. Positive and negative values indicate a contribution to the recharge and discharge of WWV respectively.



1104 FIG. 12. Depth-longitude transects across the equatorial Pacific of the vertical mixing water mass transfor-  
 1105 mation velocities  $\mathcal{G}_M$  during the 1988/89 La Niña event in the hindcast simulation. The contours show the  
 1106 distribution of the equatorial isotherms with the 20°C isotherm in bold. The dashed blue line in the upper-most  
 1107 layers indicates the mixed layer depth as defined in Fig. 4. As La Niña develops, the 20°C isotherm shifts  
 1108 upward into the surface region where enhanced vertical mixing cools water masses (blue region) and leads to  
 1109 strong downward volume flux across the isotherm into deeper layers. After the peak of the event, vertical mixing  
 1110 decreases and the isotherms return to their original position below the region where vertical mixing warms water  
 1111 masses (red region).

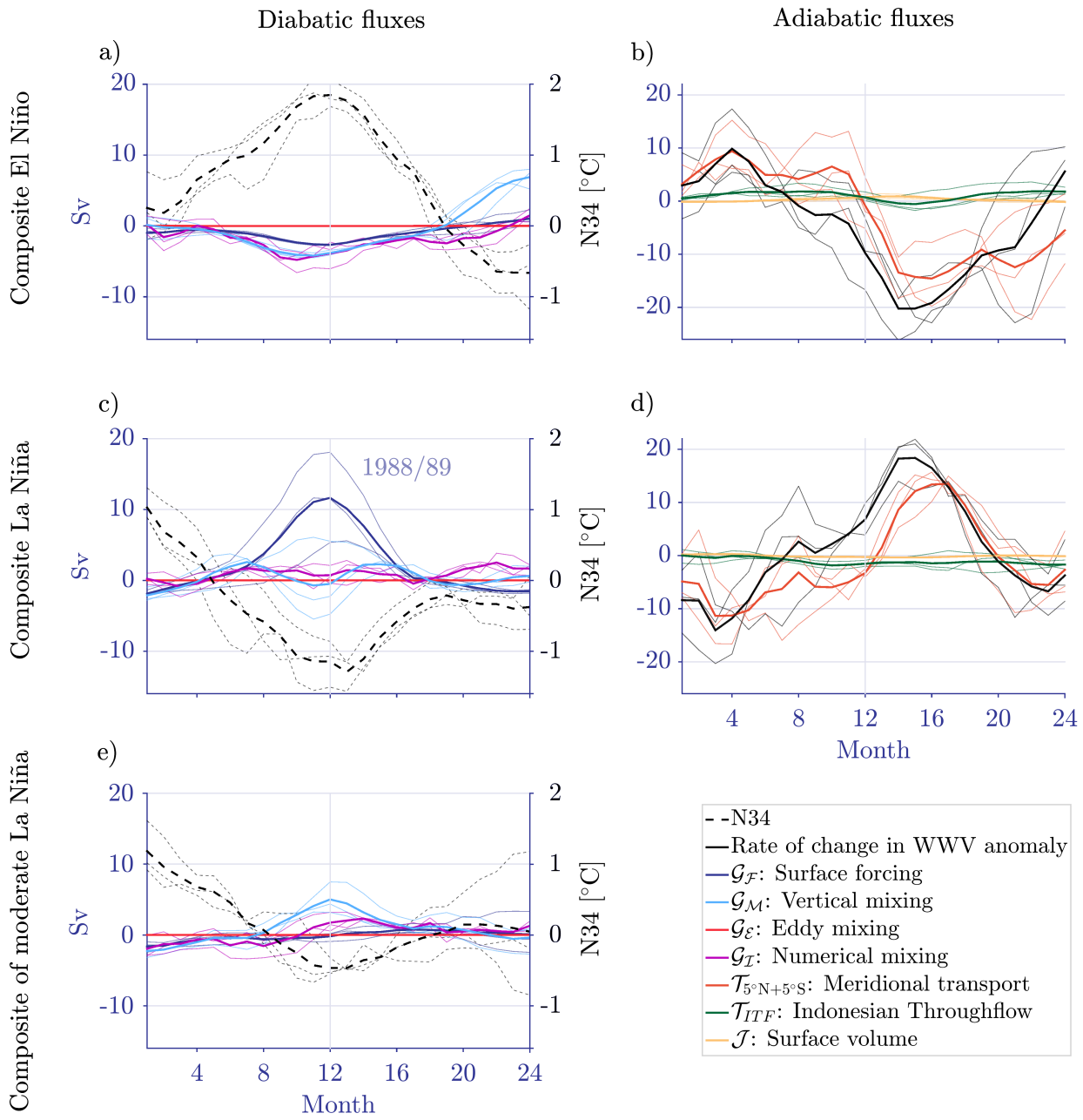


FIG. 13. Composite time series centered in December (month 12) of the (a, c) diabatic WWV budget terms as well as (b, d) the rate of change in WWV and the adiabatic terms [Sv] during the three strong El Niño and La Niña events shaded in red and blue in Fig. 11. The label 1988/89 in (c) shows the time series of the surface forcing term during the 1988/89 La Niña event. In (e) the composite diabatic time series for three moderate La Niña events in 1984/85, 1995/96, 2006/07. In the left panels we also show the time series for the N34 index [ $^{\circ}\text{C}$ ] (dashed black line). The faint lines are the time series corresponding to the three events while the solid lines are the composites.

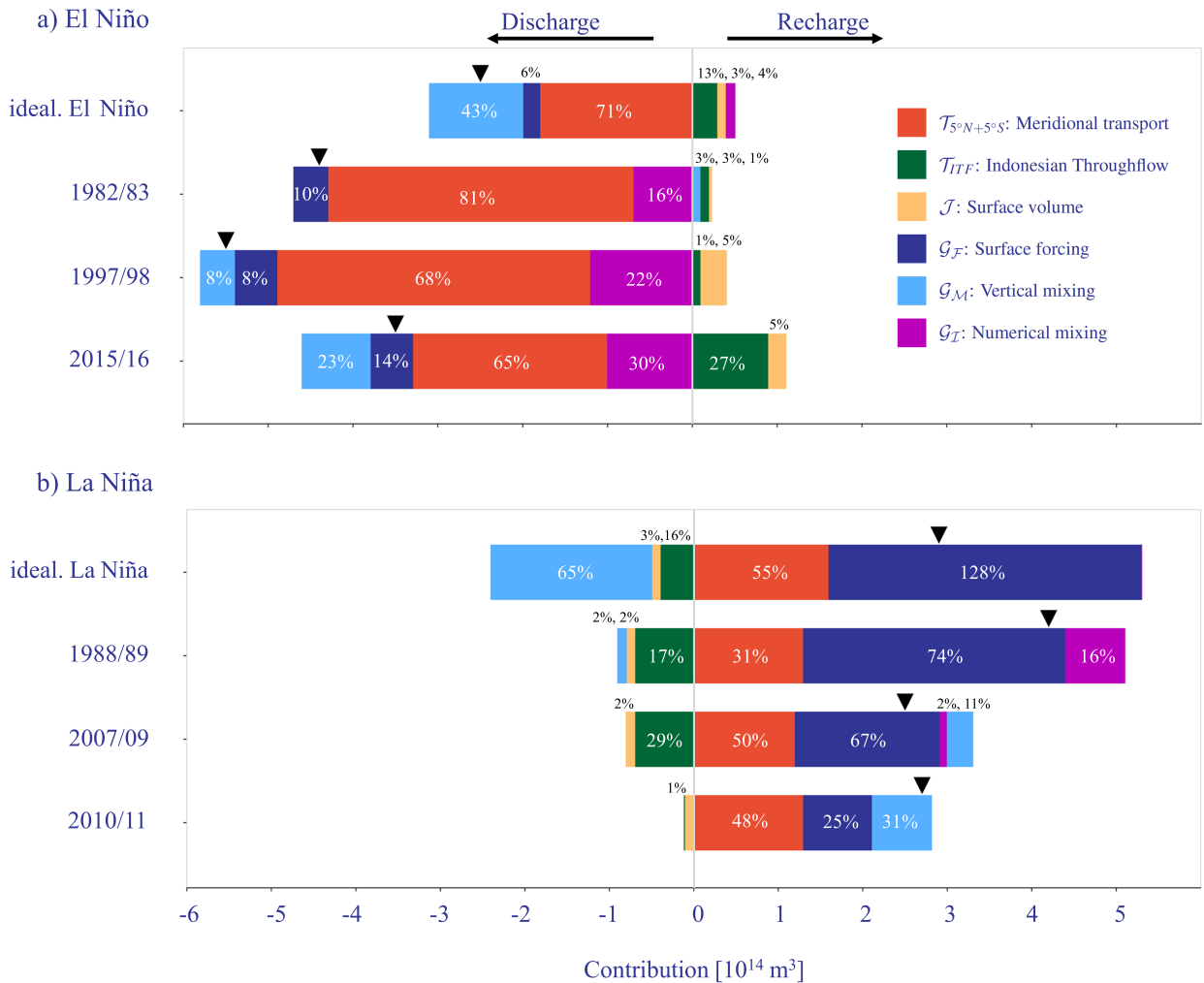


FIG. 14. The total time-integrated contribution of each anomalous WWV budget term [ $10^{14} \text{ m}^3$ ] during (a) El Niño and (b) La Niña periods as defined by the red and blue shaded periods in Fig. 6 (idealised) and Fig. 11 (hindcast). A negative value of a given flux indicates its role in discharging WWV and a positive value indicates a recharge respectively. The percentage values in each section show the time-integrated contribution to the total change in WWV and are calculated from values rounded to 1-digit accuracy. The triangular markers show the total change in WWV over a particular event.

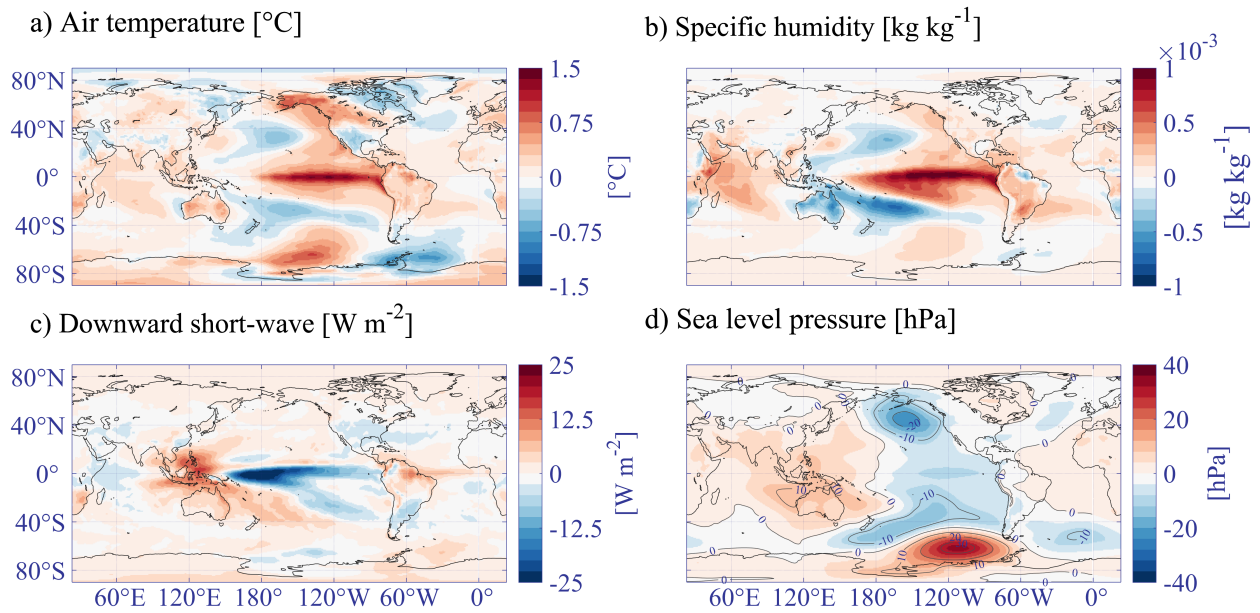


Fig. A1. Examples of four out of the eight atmospheric regression patterns  $X_1$  associated with ENSO used in the atmospheric forcing for the idealised symmetric events. These spatial patterns are calculated by regressing the observed N34 index (Reynolds et al. 2007) onto anomalous spatial maps from the ERA-Interim reanalysis product for 1979–2016 (Dee et al. 2011) and taking the time mean. (a) Air temperature [ $^{\circ}\text{C}$ ], (b) specific humidity [ $\text{kg kg}^{-1}$ ], (c) downward short-wave radiation [ $\text{W m}^{-2}$ ] and (d) sea level pressure [Pa].